Fibroblast-IL-7 feedback drives PDPN^{+} monocytes to restrain CD4^{+} T cell responses

Yan Fu[1,2], Christophe Toussaint[3], Ina Sauerland[1,2], Elisabeth Reiß[1,2], Lars Philipsen[4], Patricia Gintschel[1,2], Laura Knop[2,5], Andreas Braun[2,6], Bastian Kruse[2,6], Leon-Alexander Dewitz[1,2], Jonas Amore[1,2], Vladyslava Dovhan[2,5], Sönke Weinert[4], Nouria Jantz-Naeem[1,2], Iris Baars[1,2], Juliane Mohr[1,2], Julia Prein[1,2], Cora Schwendele[1,2], Philipp Bruno[2,5], Martin Böttcher[7], Nicole Gröger[8], Hannah Van Hove[9], Melanie Greter[9], Burkhard Becher[9], Sascha Kahlfuß[2,5], Burkhart Schraven[2,5], Robert Geffers[10], Thomas Tüting[2,6], Nicole Joller[11], Stephan Fricke[2,5,12], Antoine-Emmanuel Saliba[3,13,14]*, Thomas Schüler[2,5,14]*, Andreas J. Müller[1,2,14,15]*

[1] Experimental Immunodynamics, Institute for Clinical Immunology and Cell Therapeutics, Medical Faculty, Otto-von-Guericke University Magdeburg, Magdeburg, Germany.

[2] Health Campus Immunology, Infectiology and Inflammation (GCI3) and Center for Health and Medical Prevention (CHaMP), Otto-von-Guericke-University, Magdeburg, Germany

[3] Helmholtz Institute for RNA-based Infection Research, Helmholtz Centre for Infection Research, Würzburg, Germany.

[4] Platform for Multiparametric Bioimaging and Cytometry (MPBIC), Medical Faculty, Otto-von-Guericke-University, Magdeburg, Germany.

[5] Institute for Clinical Immunology and Cell Therapeutics, Medical Faculty, Otto-von-Guericke University Magdeburg, Magdeburg, Germany

[6] Department of Dermatology, Medical Faculty, Otto-von-Guericke University Magdeburg, Magdeburg, Germany.

[7] Department of Hematology, Oncology, and Cell Therapy, Medical Faculty, Otto-von-Guericke University Magdeburg, Magdeburg, Germany.

[8] Department of Zoology/Developmental Neurobiology, Institute of Biology, Otto von Guericke University Magdeburg, Magdeburg, Germany.

[9] Institute of Experimental Immunology, University of Zurich, Switzerland

[10] Helmholtz Centre for Infection Research, Braunschweig, Germany.

[11] Department of Quantitative Biomedicine, University of Zurich, Zurich, Switzerland.

[12] Fraunhofer Institute for Cell Therapy and Immunology, Leipzig, Germany.

[13] University of Würzburg, Faculty of Medicine, Institute of Molecular Infection Biology, Würzburg, Germany.

[14] These authors contributed equally

[15] Lead contact

* Correspondence: emmanuel.saliba@helmholtz-hiri.de (A.E.S.); thomas.schueler@med.ovgu.de (T.S.); andreas.mueller@med.ovgu.de (A.J.M.)

36 **Summary**

37 During immune responses, pro- and anti-inflammatory mechanisms must be balanced to ensure
38 pathogen clearance while limiting tissue damage. Monocyte-derived cells contribute to both processes,
39 yet the underlying regulatory circuits remain incompletely defined. Here, we show that a subset of
40 $PDPN^{+}IL\text{-}7R^{+}$ monocyte-derived cells that impair effector $CD4^{+}$ T cell–mediated control of intracellular
41 pathogens, and thus perpetuate the infection. Fibroblast-derived IL-7 drives this immunosuppressive
42 program, which is up-regulated in response to IFNγ. We thus uncover a cytokine-dependent feedback
43 circuit in which elevated IFNγ induces IL-7 production by fibroblasts, licensing immunosuppressive
44 monocyte-derived cells that restrain $CD4^{+}$ T cell responses. This mechanism links excessive
45 inflammation to immune suppression at the expense of pathogen control. Targeting this feedback loop
46 may enable therapeutic strategies that enhance antimicrobial immunity while preserving tissue integrity.

Introduction

Inflammation induces the recruitment of large numbers of monocyte-derived myeloid cells which phagocytose invading pathogens, deliver antimicrobial effector molecules and thus limit pathogen load. However, such cells also exert regulatory functions required for the resolution of inflammation and tissue repair (Guilliams et al., 2018). This is of critical importance for host survival, since unrestrained immune responses endanger tissue integrity and organ function (Ortega-Gomez et al., 2013; Postat et al., 2018; Sugimoto et al., 2016). Intracellular pathogens infecting monocyte-derived cells can interfere with anti-microbial effector functions of their host, thereby establishing long-term persistence and chronic disease (Carvalho et al., 2023; Collins-McMillen et al., 2017; Drewry et al., 2019; Mariotti et al., 2004; Stapels et al., 2018). Furthermore, monocyte-derived cells can acquire an immunosuppressive phenotype that counter-regulates effector functions of other immune cells, or shifts immune responses towards a less inflammatory phenotype (Gundra et al., 2017; Zhang et al., 2022). Elucidating and manipulating these diverse functions holds the potential to improve treatment for infectious diseases (Channappanavar et al., 2016; Dorhoi et al., 2014; Wallis et al., 2023) and cancer (Kruse et al., 2023; Mantovani et al., 2022) but the mechanisms by which such functions are induced and deployed remain incompletely understood.

Upon arrival in the tissue, monocytes adapt their functional properties in response to complex environmental cues, including inflammation- and pathogen-derived signals. This context-dependent adaptation is crucial for a balanced response ensuring pathogen elimination and tissue protection at the same time (Veglia et al., 2021). Thus, within a population of activated monocyte-derived cells, a mixture of pathways triggering inflammatory, antimicrobial, and tissue remodeling functions must be activated (Sanin et al., 2022). Single-cell RNA sequencing (scRNAseq) has been instrumental in dissecting monocytes and their derivatives into phenotypically and functionally distinct subpopulations during infection by intracellular bacterial (Bryson et al., 2019; Hoffman et al., 2021), viral (Baasch et al., 2021) or parasitic (Patir et al., 2020) pathogens, as well as in the tumor microenvironment (Cheng et al., 2021; Mulder et al., 2021). Some of these subpopulations have the capacity to critically divert the course of the disease, even if present only at a small number compared to the total monocyte population

75 (Hoffmann et al., 2022; Zhang et al., 2022). In the course of an infection, the level of complexity is
76 further increased by a significant diversity of virulence, growth rate and invasiveness of individual
77 pathogens, thereby additionally modulating the functional properties of the infected cell type (Avraham
78 et al., 2015; Pisu et al., 2021; Saliba et al., 2016).
79 To address the differential monocyte-derived cell functions in the context of the diverse pathogen states,
80 we employed *Leishmania major* (*L. major*) infection as a physiological model for infection-induced
81 recruitment and activation of monocytes (Heyde et al., 2018; Romano et al., 2017). In this model system,
82 monocyte-derived cells represent the preferential host cell type for intracellular pathogen proliferation
83 and, at the same time, are critical for controlling the parasite through expression of the inducible nitric
84 oxide synthase (iNOS) in response to T cell-derived Interferon-γ (IFNγ) (De Trez et al., 2009; Leon et
85 al., 2007; Muller et al., 2012; Olekhnovitch et al., 2014). Permanent monocyte recruitment to and
86 maturation at the site of infection results in a large phenotypic and functional diversity. Importantly, the
87 proliferation state of the pathogen correlates with the phenotype and function of the infected monocyte-
88 derived cells (Formaglio et al., 2021; Heyde et al., 2018; Mandell and Beverley, 2017). Also, the
89 composition and polarization of these cell populations has been shown to critically impact on the
90 deployment of the anti-*Leishmania* response, e.g. by entertaining type II immune cell circuitries (Lee et
91 al., 2023), or by modulating the reservoir of monocyte-derived cells permissive for pathogen
92 proliferation (Carneiro et al., 2020). However, the cellular and molecular interactions which enable
93 monocyte-derived populations to impact prolongation versus control of the infection remain to be fully
94 elucidated.
95 Here, we combined an *in vivo* pathogen proliferation reporter system with scRNAseq to characterize the
96 function of distinct monocyte-derived subpopulations in the context of their interactions with
97 intracellular pathogens. With the help of this approach, we identified a subset of Podoplanin (PDPN)-
98 and Interleukin-7 receptor (IL-7R) expressing cells which are derived from monocytes and preferentially
99 harbor low-proliferating *L. major*. This PDPN^{+}IL-7R^{+} population exhibited a hypo-inflammatory
100 phenotype and suppressed effector functions of *L. major*-specific CD4^{+} T cells in response to fibroblast-
101 derived IL-7. IL-7 production was dependent on IFNγ release in the course of the adaptive immune
102 response against *L. major*. Interference with IL-7R signaling or depletion of these cells, as well as *Il7*

103 gene inactivation in fibroblasts, resulted in improved effector T cell responses and subsequent pathogen
104 clearance.
105 In summary, we provide evidence for an as-yet unknown feedback loop which dampens T cell responses
106 as a result of the inflammation-associated up-regulation of fibroblast-derived IL-7, and the subsequent
107 immunosuppressive activity of IL-7R^{+} monocyte-derived cells. This mechanism can favour the
108 pathogen to establish persistence and could therefore represent a new target for immunotherapeutic
109 approaches.
110

111 **Results**

112

113 **PDPN^{+}IL-7R^{+} phagocytes infected with low proliferating *L. major* exhibit a hypo-inflammatory**
114 **phenotype**

115 During local immune responses, tissue- and inflammation-derived signals modulate the phenotype and
116 function of recruited immune cells (Romano et al., 2017; Saliba et al., 2016; Szabo et al., 2021; Yamada
117 et al., 2020). However, dissecting these environmental cues has remained challenging. We and others
118 have shown previously that intracellular *L. major* proliferation differs considerably between infected
119 monocyte-derived cells recruited to the infection site (Heyde et al., 2018; Mandell and Beverley, 2017).
120 We therefore utilized pathogen proliferation rate as a proxy for host-pathogen interaction cues which
121 define distinct monocyte-derived cell functions *in vivo*. For this, we employed an *in vivo* proliferation
122 assay, which relies on genetically modified *L. major* parasites expressing the photoconvertible green
123 fluorescence protein mKikume (Lm^{SWITCH}). Upon illumination, mKikume molecules convert from green
124 to red. Consequently, red molecules are preserved in low-proliferating parasites (Lm^{lo}), but are diluted
125 by newly synthesized green molecules in high-proliferating *L. major* (Lm^{hi}) (Fig. 1A) (Formaglio et al.,
126 2021).

127 To characterize the transcriptome of cells which harbour Lm^{lo} and Lm^{hi}, we infected C57BL/6 (B6) mice
128 with 2 x 10^{6} Lm^{SWITCH} in the ear. At 19 days post infection (p.i.), the parasites were photoconverted and
129 CD45^{+} leukocytes were MACS purified 2 days later from the infected ear. Subsequently, single-cell
130 sorting of uninfected, Lm^{lo}- or Lm^{hi}-containing monocyte-derived cells was performed (Fig. 1B). Both
131 CD11c^{int-hi} and Ly6c^{+} were selected to cover a broad spectrum of recruited monocyte-derived cells (Fig.
132 S1A) (Heyde et al., 2018; Olekhnovitch et al., 2014). Lm^{lo}- or Lm^{hi}-infected (termed Lm^{lo}Mo or Lm^{hi}Mo,
133 respectively) as well as uninfected (termed UMo) single monocyte-derived cells were separated using
134 index-sorting into individual wells (Fig. 1C and S1B). ScRNAseq using the SMARTseq2 protocol
135 (Picelli et al., 2013) revealed specifically and consistently high *L. major* transcript counts in cells sorted
136 as infected, but not uninfected (Fig. 1D). In total, 88% of the sorted cells had passed quality control
137 based on mitochondria read counts and percentage of ERCC (Fig. S1C, and see details in Methods).

138 Mapping of the sequenced cells sorted as *Lm*^{hi}Mo (green), UMo (black) and *Lm*^{lo}Mo (red) to a batch-
139 corrected Uniform Manifold Approximation and Projection (UMAP) representation (Fig. 1E, S1D, and
140 S1E) revealed that cells infected with *Lm*^{lo} exhibited a unique gene expression profile. In contrast,
141 uninfected cells and cells infected by *Lm*^{hi} were not distinguishable on the UMAP representation.
142 Unsupervised clustering using the Leiden algorithm identified three distinct clusters of cells referred to
143 as Cluster 1, 2 and 3, with Cluster 3 consisting mainly of *Lm*^{lo}Mo, (Fig. 1F; Table S1).
144 Gene ontology (GO) function terms revealed a differential regulation of mainly immune system-related
145 processes for Cluster 3, but not Cluster 1 and 2. In particular, biological process enrichment in Cluster
146 3 included immunosuppressive signaling pathways, but lowered immune-activating functions and
147 antigen processing as compared to Cluster 1 and 2 (Fig. S1F-G; Table S2-3). Regarding differentially
148 expressed genes (DEG) specific for Cluster 3, we found a strong reduction of the proinflammatory
149 cytokine gene *Il1b*, chemokines and class II MHC-related genes as compared to Cluster 1 and 2. In
150 contrast, cathepsins and immune checkpoint ligands were expressed specifically in Cluster 3, in line
151 with a hypo-inflammatory phenotype suggested by GO terms. Moreover, we found a specific expression
152 of *Pdpn* in Cluster 3, which is reported to be involved in immunomodulatory functions of myeloid cells
153 (Hovd et al., 2024; Rayes et al., 2017). Additionally, *Il7r* was strongly upregulated in Cluster 3. In
154 contrast, *Ccr2* expression was virtually absent in this population (Fig. S1H).
155 As Cluster 3 consisted mainly of *Lm*^{lo}Mo, while *Lm*^{hi}Mo and UMo were evenly dispersed across Cluster
156 1 and 2 (see Fig. 1E), we defined the five most prominent populations for further analysis, i.e. *Lm*^{hi}
157 infected and uninfected cells in Cluster 1 (termed *Lm*^{hi}Mo1 and UMo1) and Cluster 2 (termed *Lm*^{hi}Mo2
158 and UMo2), as well as cells infected with *Lm*^{lo} in Cluster 3 (termed *Lm*^{lo}Mo3) (Fig. 1G). The gene
159 expression pattern specific for Cluster 3 (see Fig. S1H) was consistent with the comparison of *Lm*^{lo}Mo3
160 versus *Lm*^{hi}Mo1, UMo1, *Lm*^{hi}Mo2 and UMo2 (Fig. 1H). This notably included the significantly higher
161 expression of *Pdpn* and *Il7r*, suggesting that PDPN^{+}IL-7R^{+} *Lm*^{lo}Mo3 constitute a hypo-inflammatory
162 cellular subset. These observations were validated by cells sorted according to their differential
163 expression of CD11c (high in Cluster 1), Ly6c (high in cluster 2, intermediate in infected cluster 1)
164 observed during index sorting, and CCR2 (high in cluster 2) observed in scRNAseq (Fig. S1I, and S1J).
165 Quantitative PCR (qPCR) of cells sorted based according to this strategy (Fig. S1K) reproduced the

166 differential gene expression of *Lm*^{lo}Mo3 observed in scRNAseq, including the specific expression of
167 *Pdpn* and *Il7r*, and the hypo-inflammatory phenotype indicated by lower expression of *Il1b*, *Il1r2* and
168 *Ccl5* (Fig. S1I). Also, *Lm*^{lo}Mo3 exhibited the lowest levels of pro-IL-1β, CXCL9 protein among all five,
169 and the lowest IL-6 and IL-12 p35 protein among the infected cell subsets (Fig. 1J). Irrespective of
170 whether we gated *Lm*^{lo}Mo3 cells from the infection gated according to CD11c, Ly6C and CCR2 (see
171 Fig. S1K), or as CD11b^{+}Ly6G^{-}SiglecF^{-} monocytes gated for PDPN and IL-7R expression, *Lm*^{lo}Mo3,
172 PDPN^{+}IL-7R^{+} monocytes, respectively, exhibited a low intracellular pathogen proliferation rate (Fig.
173 S1L-N). These data altogether suggested a PDPN^{+}IL-7R^{+} phagocyte population which is infected with
174 low proliferating *L. major* and which exhibits a hypo-inflammatory phenotype.
175 Recently we demonstrated similarities between monocyte-derived cell activation during the immune
176 response against *L. major* and skin melanoma (Kruse et al., 2023). Accordingly, we also detected a
177 monocyte-derived cell population expressing IL-7R and PDPN in skin melanoma at a rate comparable
178 to monocyte-derived cells in the *Leishmania*-infected skin (Fig. S2A-B). Unsupervised Leiden
179 clustering of published single-cell transcriptome data from tumor-associated monocyte-derived cells
180 (Kruse et al., 2023) confirmed the presence of an *Il7r* and *Pdpn*-expressing monocyte-derived
181 population (Figure S2C). This population exhibited a very similar transcriptional pattern as Cluster 3
182 from *L. major* infected mice (Figure S2D-E, Table S4-5, see also figure S1G-H for comparison),
183 suggesting the occurrence of IL-7R^{+}PDPN^{+} hypo-inflammatory monocyte-derived cells beyond
184 infection settings.
185 These data altogether suggested a PDPN^{+}IL-7R^{+} phagocyte population in the inflamed skin which
186 exhibits a hypo-inflammatory phenotype.
187
188
189 **IL-7R^{+}PDPN^{+} *Lm*^{lo}Mo3 develop from bone-marrow derived CCR2^{+} monocytes and acquire their**
190 **phenotype in the infected tissue**
191 To further characterize the IL-7R^{+}PDPN^{+} *Lm*^{lo}Mo3, we analyzed mannose receptor (CD206) and FcγRI
192 (CD64) expression, which distinguished tissue-resident macrophages, dendritic cells as well as different
193 stages of inflammatory monocytes and monocyte-derived macrophages (Carneiro et al., 2020; Lee et

194 al., 2018; Lee et al., 2023) (Fig. 2A and S3A). Infected IL-7R^{+}PDPN^{+} phagocytes consisted mainly of
195 Ly6C^{int} monocyte-derived macrophages, but hardly any tissue-resident and monocyte-derived dendritic
196 cells (TR/MoDC), nor tissue-resident macrophages (TRM) (Fig. 2B and S3B). The same was observed
197 when analyzing phagocytes infected with low proliferating *L. major* (Fig. 2B and S3C-D). Thus
198 independently of the gating strategy, IL-7R^{+}PDPN^{+} *Lm*^{lo}Mo3 cells seemed to consist mainly of Ly6C^{int-}
199 ^{lo}, monocyte-derived macrophages.
200 Having shown a monocyte-derived phenotype, we sought to determine the dynamics of IL-7R^{+}PDPN^{+}
201 *Lm*^{lo}Mo3 recruitment and turnover. For this, we employed optical time-stamping with mKikume-
202 transgenic mice, in which photoconversion allows the identification of cells recruited before and after a
203 distinct time point (Formaglio et al., 2021; Heyde et al., 2018). The mice were infected with *L. major*
204 expressing blue-fluorescent mTurquoise (*Lm*^{Turquoise}), and mKikume-expressing host cells in the ear were
205 photoconverted at 16 dpi, and analyzed by flow cytometry 5 days later (Fig. 2C). This allowed
206 determining IL-7R and PDPN expression in infected cells and to discriminate photoconverted, long
207 resident (recruited > 5 days before analysis) cells from short resident cells which had been recruited
208 after photoconversion (Fig. 2D and S3E). Importantly, PDPN^{+}IL-7R^{+} cells were found nearly
209 exclusively in the long resident cell fraction, while all other monocyte-derived cells exhibited a higher
210 turnover rate and were recruited mainly after the photoconversion (Fig. 2D and E).
211 Because of their long tissue residence time, we aimed to formally demonstrate whether or not *Lm*^{lo}Mo3
212 derive from CCR2^{+} monocytes. For this, we employed lethally irradiated mice reconstituted with Ccr2-
213 creERT2 (Croxford et al., 2015) x Ai14 (Rosa-CAG-LSL-tdTomato-WPRE) BM, in which *Ccr2*-
214 expressing cells permanently express red fluorescent tdTomato upon Tamoxifen treatment. Tamoxifen
215 was applied either before the infection in order to label cells recruited during the innate wave of
216 monocyte recruitment, or from day 11 p.i. in order to label monocytes recruited during the established
217 adaptive immune response (Carneiro et al., 2020) (Fig. 2F). Tamoxifen treatment induced robust
218 labeling of >75% of blood monocytes for several days (Fig. 2G and S3F). In the infected ear, all
219 monocyte-derived populations, including PDPN^{+}IL-7R^{+}, showed a large proportion of CCR2-dependent
220 tdTomato expressing cells if Tamoxifen was applied during the adaptive wave of monocyte recruitment,
221 but not if the innate wave of monocytes was labeled (Fig. 2H, S3G-H). Therefore, we concluded that

222 despite its low turnover rate as compared to other monocyte-derived cells, the PDPN^{+}IL-7R^{+} *Lm*^{lo}Mo3
223 population was derived from CCR2^{+} inflammatory monocytes recruited to the site of infection.
224
225 **PDPN^{+}IL-7R^{+} *Lm*^{lo}Mo3 dampen T cell responses against *L. major* infection *in vivo***
226 Having shown IL-7R and PDPN expression for monocyte-derived cells in the infected ear, we assessed
227 whether other immune cell types at the infection site, in particular non-myeloid cells, might also include
228 PDPN^{+}IL-7R^{+} double-positive cells (Fig. S4A-C). While as expected, IL-7R was expressed on several
229 leukocyte subsets, PDPN expression, and, consequently, PDPN and IL-7R double-expression, was
230 limited to monocyte-derived, in particular infected, cells (Fig. 3A).
231 Since all IL-7R^{+} monocyte-derived cells co-expressed PDPN, we next employed a *Pdpn-cre* based BM
232 reconstitution approach to specifically abolish IL-7R in these cells (Fig. 3B). For this, we lethally
233 irradiated WT recipient mice, reconstituted them with either *Pdpn-cre* × *Il7r*$^{fl/fl}$ or littermate BM, and
234 infected them with *Lm*^{DsRed} 10 weeks after reconstitution. Pathogen control and effector T cell activation
235 were analyzed at week 3 p.i. We found that IL-7R was significantly diminished in *Lm*^{lo}Mo3, but not in
236 lymph node T cells, confirming monocyte-specific gene deletion of *Il7r* (Fig. 3C and S4D). Strikingly,
237 the *Pdpn-cre* dependent *Il7r* knockout on BM-derived cells significantly reduced *L. major* infected
238 monocytes and pathogen burden (Fig. 3D and S4E). Furthermore, IFNγ production in effector CD4^{+} T
239 cells within the infected ear tissue was elevated (Fig. 3E and S4F), suggesting that disruption of IL-7R
240 signaling in monocyte-derived cells at the site of infection enhances pathogen control by the adaptive
241 immune response. We were able to reproduce the enhanced pathogen control in a different experimental
242 system by reconstituting irradiated recipients with *Rag1*$^{-/-}$× *Il7r*$^{-/-}$ BM and adoptive transfer of WT CD4^{+}
243 (Fig. S4G). The resulting animals, in which IL-7R was exclusively present on lymphocytes, also
244 exhibited enhanced control of *L. major,* confirming the role of IL-7R signaling in non-lymphocyte
245 immune cells (Fig. S4H-I).
246 Enhanced pathogen control in the absence of IL-7R signaling in monocyte-derived cells could be due to
247 cell-intrinsic enhancement of intracellular pathogen control in individual cells devoid of IL-7R, or due
248 to cell-extrinsic effects. In order to address these possibilities, we generated mixed BM chimeras
249 reconstituted with 50% CD45.1 WT and 50% *Il7r*$^{-/-}$ (CD45.2) BM. Mice reconstituted with mixtures of

250 WT CD45.1 and WT CD45.2 BM served as controls (Fig. 3F). We found that infection rates (Fig. 3G),
251 the relative abundance, (Fig. 3H), and the parasite proliferation within (Fig. 3I) the different monocyte-
252 derived cell subsets were independent of the cellular *Il7r* genotype in the mixed BM chimeras.
253 Therefore, we concluded that IL-7R signaling in the IL-7R^{+}PDPN^{+} *Lm*^{lo}Mo3 does not affect their
254 development, abundance, or cell-intrinsic defense function, but dampens pathogen control in a cell-
255 extrinsic manner.
256 Next, we aimed to assess the effect of the depletion of PDPN^{+}IL-7R^{+} *Lm*^{lo}Mo3 on the control of *L.*
257 *major*. For this, we crossed *Pdpn-cre* transgenic mice to iDTR mice expressing the Diphtheria Toxin
258 receptor (DTR) after Cre-mediated elimination of a DNA-STOP cassette (Buch et al., 2005). Using these
259 mice as donors, we created BM chimeras reconstituted with 100% *Pdpn-cre* × iDTR, as well as controls
260 reconstituted with mixed 50% WT (CD45.1) and 50% *Pdpn-cre* × iDTR (CD45.2) BM (Fig. 3J).
261 Diphtheria Toxin (DTX) treatment of mice reconstituted with *Pdpn-cre* × iDTR BM reduced
262 significantly the percentage PDPN^{+} cells among infected phagocytes (Fig. 3K), indicating successful
263 depletion at the site of infection. Importantly, the percentage of infected cells, as well as *L. major* tissue
264 burden was significantly reduced in these animals as compared to non-depleted of only partially
265 depletable BM chimera reconstituted with 50% WT and 50% *Pdpn-cre* × iDTR BM (Fig. 3L and S4J).
266 Of note, this depletion was also associated with an elevated IFNγ production by CD4^{+} effector T cells
267 (Fig. 3M and S4K). These results underlined an immunosuppressive function of PDPN^{+}IL-7R^{+} *Lm*^{lo}Mo3
268 in promoting parasite persistence via the inhibition of CD4^{+} T effector functions. Thus, we concluded
269 that IL-7R signaling in *Lm*^{lo}Mo3 ultimately resulted in a dampened T cell response against *L. major* and
270 impaired pathogen control.
271

272 **IL-7 from IFNγ-induced fibroblasts establishes a feedback loop that limits the effector T cell**
273 **response in the skin**

274 Stromal cells, particularly fibroblasts, have been shown to produce IL-7 in response to *L. major* infection
275 (Peduto et al., 2009). In line with this, we found that fibroblasts from infected *Pdpn-cre* × *Il7r*$^{fl/fl}$ BM
276 reconstituted tissues expressed more MHC-I and PD-L1 than controls, indicating their additional
277 activation due to the enhanced immune response (Figure 4A and S5A). The same was observable in

278 *Pdpn-cre* × iDTR BM chimeric mice in which PDPN$^+$ leukocytes were depleted (Fig. 4A and S5B). Of
279 note, we found that *Il7* gene expression was upregulated in the tissue upon *L. major* infection (Fig. 4B
280 and S5C). We therefore sought to elucidate if skin fibroblasts could represent the source of the IL-7
281 modulating the immunosuppressive function of PDPN$^+$IL-7R$^+$ *Lm*^{lo}Mo3. For this, we employed *Prrx-*
282 *cre* × *Il7*$^{fl/fl}$ mice, which lack *Il7* gene activity in fibroblasts (Knop et al., 2020). Quantitative PCR of
283 stromal cells sorted from the ear confirmed that *Prrx* expression was limited to fibroblasts (Fig. 4C),
284 which were also more abundant in the infected skin than vascular endothelial cells (Fig. 4D and S5D).
285 Additionally, *Il7* expression was significantly reduced in fibroblasts from infected *Prrx-cre* × *Il7*$^{fl/fl}$
286 mouse ear tissue, but not in any other stromal cell population, further confirming a fibroblast-specific
287 *Il7* gene deficiency (Fig. 4E-F). This suggested that *Prrx-cre* × *Il7*$^{fl/fl}$ mice indeed lacked *Il7* primarily
288 in fibroblasts in the infected tissue, and that fibroblasts are present in high numbers as compared to
289 vascular endothelial cells as alternative producers of IL-7 (Hara et al., 2012). Importantly, *L. major*
290 clearance was enhanced in *Prrx-cre* × *Il7*$^{fl/fl}$ mice (Fig. 4G) and IFNγ production by CD4$^+$ T cells was
291 increased (Fig. 4H and S5E). This suggested that fibroblast-derived IL-7 was involved in the suppression
292 of the immune response against *L. major*.
293 IFNγ has been reported to induce IL-7 expression in skin fibroblasts (Dai et al., 2021). Therefore, we
294 hypothesized that enhanced IFNγ production by T cells may contribute to a fibroblast-associated
295 feedback loop, limiting the effectiveness of an initially productive T cell response. This may be a result
296 of IL-7 induction by fibroblasts finally leading to immunosuppression of T cells by PDPN$^+$IL-7R$^+$
297 *Lm*^{lo}Mo3 and subsequent pathogen persistence. In line with this hypothesis, we had shown previously
298 that IFNγ from T cells alone is sufficient for *L. major* containment (Muller et al., 2012), and found T
299 cells represented the main IFNγ producing cell population (Fig. 5A and S6A-B). Also, fibroblasts
300 cultured in the presence of recombinant IFNγ exhibited increased *Il7* cytokine gene expression (Fig.
301 5B). This suggested that T cell-derived IFNγ could stimulate fibroblasts in the infectious environment
302 to produce IL-7.
303 In order to demonstrate the impact of IFNγ signaling on IL-7 production by fibroblasts in vivo, we
304 treated *L. major*-infected mice with IFNγ-specific blocking or isotype-matched control antibodies (Fig.
305 5C). In fibroblasts from the infected tissue of control mice, we observed a strong correlation between

306 *Il7* gene expression and the cellular infection rate. In contrast, this correlation was lost after anti-IFNγ
307 treatment (Fig. 5D). Consequently, anti-IFNγ treatment reduced fibroblasts *Il7* expression in strongly
308 infected tissues (Fig. 5E), and decreased fibroblast activation (Fig. 5F and S6C). Therefore, we
309 concluded that the IFNγ produced during the T cell response against *L. major* induces IL-7 production
310 in fibroblasts, thereby activating immunosuppressive PDPN^{+}IL-7R^{+} *Lm*^{lo}Mo3 which subsequently blunt
311 pathogen clearance.
312
313 **Anti-IL-7/IL-7R treatment results in an enhanced immune response against *L. major***
314 Our data suggested that targeting IL-7R signaling might offer a possibility to prevent
315 immunosuppression by PDPN^{+}IL-7R^{+} *Lm*^{lo}Mo3, thus enhancing effector T cell responses and reducing
316 pathogen burden. Sustained long-term treatment with anti-IL-7R antibody has been shown to impair T
317 cell responses (Colpitts et al., 2009). However, IL-7R has been reported to be critical for maintaining
318 mainly naïve and memory T cells, but less important for effector T cells (Capitini et al., 2009; Fry and
319 Mackall, 2002; Huster et al., 2004). Thus, IL-7/IL-7R-blockade could suspend immunosuppression by
320 PDPN^{+}IL-7R^{+} *Lm*^{lo}Mo3 when applied temporarily during the acute infection.
321 To test if such transient anti-IL-7/IL-7R treatment improves the control of *L. major* infections, we
322 injected *L. major*^{DsRed}-infected mice with an anti-IL-7/IL-7R antibody cocktail after the establishment
323 of infection (Fig. 6A). As expected for IL-7-depleting conditions (Grabstein et al., 1993), the treatment
324 resulted in a decline of immature B cells in the BM and spleen, but not in mature B cells (Fig. S7A-B)
325 three days after antibody injection. We also observed a slight reduction in total CD4^{+} T cells, while the
326 numbers of central memory, effector or regulatory T cells were unchanged in the draining lymph node
327 (Fig. S7C). This indicated that the short-term treatment did not profoundly affect the peripheral
328 lymphocyte homeostasis, or T cell effector populations. Importantly, anti-IL-7/IL-7R treatment resulted
329 within 3-5 days in strongly reduced *L. major* infection (Fig. 6B-C), enhanced IFNγ production by
330 effector T cells (Fig. 6D and S7D), and increased fibroblast activation (Fig.6E and S7E) in the skin. To
331 explore whether anti-IL-7/IL-7R blockade also increased the induction of IFNγ-dependent antimicrobial
332 effector functions (Muller et al., 2012), we determined iNOS expression in monocyte-derived cells
333 isolated from the site of infection and found that anti-IL-7/IL-7R treatment resulted in higher iNOS

334 expression in these cells (Fig.6F and S7F). Collectively, these data indicated that IL-7/IL-7R blockade
335 efficiently increased the adaptive immune response against established skin infections with *L. major*.
336 In order to address whether impaired IL-7R signaling had a long-term effect on pathogen control, and
337 immune activation, we analysed the impact of anti-IL-7/IL-7R treatment several weeks after antibody
338 treatment. For this, *L. major*^{DsRed} infected mice were injected with anti-IL-7/IL-7R antibody or isotype
339 control at day 16 and 20 p.i., and analyzed at week 7 p.i. for pathogen control and immune activation
340 (Fig. 6G). Weekly measurement of the infected ear thickness indicated a transiently higher inflammation
341 in anti-IL-7/IL-7R injected versus control animals, suggesting that the treatment increased the amplitude
342 of the immune response (Fig. 6F). At week 7 p.i., *L. major* tissue burden was reduced compared to
343 isotype control-treated animals (Fig. 6I), indicating that although the local pathology seemed
344 comparable at this late time point, the transient anti-IL-7/IL-7R had a lasting effect on pathogen control.
345 Furthermore, the fraction of IFNγ-producing effector T cells was strongly increased in the draining
346 lymph nodes of anti-IL-7/IL-7R treated animals (Fig. 6J and S7G). These data suggested that the
347 transient blockade of IL-7/IL-7R and suspension of the immunosuppressive function of *Lm*^{lo}Mo3 in the
348 early phase of the response supported a long-lived CD4^{+} T cell response and pathogen control.
349 Altogether, our data therefore indicate that the IL-7 produced by fibroblasts in response to IFNγ drives
350 PDPN^{+}IL-7R^{+} *Lm*^{lo}Mo3 cells blunting CD4^{+} T-cell effector functions, and targeted manipulation of this
351 pathway can facilitate robust anti-*Leishmania major* immunity.
352

353 **Discussion**

354

355 Mechanisms that restrict overshooting effector functions are an important component of immune
356 responses to prevent immunopathological tissue damage (Formaglio et al., 2021; Mishra et al., 2013;
357 Postat et al., 2018; Sugimoto et al., 2016). As such, the effects of IFNγ, a main mediator of cellular
358 immune responses, are controlled on different levels, including the restriction of IFNγ-producing cells
359 (Badovinac et al., 2003) and inhibition of IFNγ signaling (Alexander et al., 1999; Marine et al., 1999).
360 Pathogens can benefit from such regulatory mechanisms to establish efficient infection (Collins-
361 McMillen et al., 2017; Dolgachev et al., 2014; Drewry et al., 2019; Mariotti et al., 2004; Navarro et al.,
362 2011), and also immune responses against tumors can be hampered by mechanisms that restrict IFNγ
363 function (Janson et al., 2008). A better understanding of the cellular and molecular interactions
364 underlying these immunosuppressive functions would greatly facilitate the development of novel
365 immunotherapeutic approaches (Gocher et al., 2022; Wykes and Lewin, 2018). Such approaches have
366 so far mainly focused on T cell functions directly, especially for the treatment of cancer (Ellis et al.,
367 2021), while the potential of monocyte-derived functions is only beginning to be acknowledged (Kruse
368 et al., 2023; Mantovani et al., 2022). We describe here a new self-limiting mechanism by which
369 increasing IFNγ levels initiate a feedback loop that ultimately prompts IL-7R expressing monocyte-
370 derived cells to prevent effector T cells from producing more IFNγ. Interruption of this feedback loop
371 increased effector T cell function and promoted pathogen clearance.
372 Our unbiased identification of a PDPN$^+$IL-7R$^+$ monocyte-derived subset that harbors low-proliferating
373 *L. major* and suppresses CD4$^+$ T-cell effector function adds a new layer to the picture of myeloid cell
374 heterogeneity during chronic infection. The plasticity of myeloid cells at infection sites has been
375 intensely studied, with ample evidence for immunomodulatory functions, for example PD-L2$^+$CD206$^+$
376 monocyte-derived macrophages in the context of helminth infection (Gundra et al., 2017; Gundra et al.,
377 2014; Oyesola et al., 2023), or CD206$^+$ tissue resident macrophages which promote type 2 immunity in
378 non-healing *L. major* Seidman strain infection (Lee et al., 2018; Lee et al., 2020; Lee et al., 2023).
379 Furthermore, CCR2$^+$ monocytes have been shown adopt a dual role in the establishment of parasite-
380 permissive conditions and the activation of parasite control depending on their time point of recruitment

381 and exposure to the local cytokine milieu (Carneiro et al., 2020). Our data extend these concepts by
382 demonstrating that, downstream of IFNγ, stromal fibroblasts secrete IL-7 that engages IL-7R on a
383 PDPN^{+} monocyte-derived population, driving these cells towards a hypo-inflammatory phenotype
384 which dampens CD4^{+} T cell responses.

385 We clearly show that PDPN^{+}IL-7R^{+} *Lm*^{lo}Mo3 cells originate from CCR2^{+} monocytes and have a
386 turnover rate of far more than five days, and do not express TRM markers such as CD206. Thus, we
387 conclude that the functional overlap with alternatively activated CD206^{+} tissue-resident macrophages
388 described previously is at most partial, and that the PDPN^{+}IL-7R^{+} *Lm*^{lo}Mo3 adopt their phenotype upon
389 exposure to the infection site. In line with this, previous reports indicate that both macrophages and
390 monocytes can upregulate cell surface expression of PDPN and IL-7R in response to inflammatory
391 stimuli (Hou et al., 2010; Kerrigan et al., 2012; Yazdani et al., 2024).

392 IL-7R expression by myeloid cells has been shown to promote the development of tissue-resident
393 macrophages in early ontogeny in mice (Cool et al., 2020; Leung et al., 2019). In humans, monocyte-
394 derived lung macrophages have been reported to express IL-7R during their development under non-
395 inflammatory conditions (Evren et al., 2021), and upregulate IL-7R expression in response to
396 inflammation (Al-Mossawi et al., 2019; Hu et al., 2008). Consequently, IL-7R expressing myeloid cells
397 were observed in a variety of inflammatory and infectious diseases. For example, serum from patients
398 infected with *Mycobacterium tuberculosis* (Mtb) as well as Mtb products induces IL-7R on monocytes
399 (Harelimana et al., 2022). Furthermore, a role of IL-7R in monocytes in modulating the immune
400 response has been suggested in human patients of SARS COV2 infection, where their presence in the
401 blood was correlated with lower disease pathology (Zhang et al., 2022). Our analysis of skin melanoma
402 tissue and re-analysis of published tumor-associated scRNAseq data suggests the presence of PDPN^{+}IL-
403 7R^{+} hypo-inflammatory monocyte-derived cells also in the inflamed tumor microenvironment. In line
404 with this, *PDPN* and *IL7R* expression was found in monocyte-derived subpopulations of human head
405 and neck carcinoma (Hoffmann et al., 2022), and *IL7R* was found to be a signature gene for tumor-
406 associated monocyte-derived cell subsets in a variety of malignancies (Cheng et al., 2021; Mulder et al.,
407 2021; Nalio Ramos et al., 2022). Altogether, these findings suggest a more general role for IL-7R
408 expressing monocyte-derived cells in dampening immune responses in a variety of diseases. With the

409 identification of a feedback loop fueled by IFNγ, which induces IL-7 production by activated fibroblasts,
410 we provide a multicellular interaction network for the immunosuppressive function of PDPN^{+}IL-7R^{+}
411 *Lm*^{lo}Mo3. Of note, we also observed PDPN^{+}IL-7R^{-} single-positive monocyte-derived cells. These cells
412 might represent an intermediate state, but, alternatively, might deploy immunoregulatory functions
413 independently of the described IL-7 dependent feedback switch, since not only IL-7R, but also PDPN
414 has been shown to be involved in immunoregulatory mechanisms (Xie et al., 2020).
415 The enhancement of pathogen clearance in response to i) *Il7r* deficiency in or depletion of PDPN^{+}IL-
416 7R^{+} *Lm*^{lo}Mo3, ii) fibroblast-specific *Il7* gene inactivation, and iii) IL-7/IL-7R blockade, strongly
417 suggests that IL-7 can mediate an immunosuppressive function. While other cell types could also
418 produce IFNγ to enhance pathogen control, T cells seem to be a main and sufficient IFNγ producer for
419 iNOS induction (Muller et al., 2012), and thereby a very likely target of the described feedback
420 mechanism. At first sight this appears counter-intuitive, since IL-7 stimulates T cell immunity at
421 multiple levels, such as thymic T cell development and the survival of naïve and memory T cells in the
422 periphery. However, this is not the case for effector T cells, which down-regulate IL-7R expression and
423 are thus insensitive to direct IL-7 effects (Bachmann et al., 2005; Huster et al., 2004; Kaech et al., 2003).
424 Importantly, endogenous IL-7 had previously been shown to suppress IFNγ production and to exacerbate
425 disease in a skin infection model of mice with *Schistosoma mansoni* (Wolowczuk et al., 1997).
426 Moreover, treatment with recombinant IL-7 can aggravate *L. major* infection in susceptible mice
427 (Gessner et al., 1995). In line with these reports, we found that short-term blockade of IL-7/IL-7R affects
428 the number of naïve T and B cells in secondary lymphoid organs, but not of effector T cells, whose IFNγ
429 production is increased, resulting in enhanced control of the pathogen. We have shown previously that
430 even slight manipulation of pathogen permissiveness at week 3 p.i. results in enhanced control later on
431 (Formaglio et al., 2021). In line with this, we observed an altered course of pathology, with stronger ear
432 swelling 2-3 weeks after anti-IL-7/IL-7R treatment. The treatment also resulted in more efficient
433 pathogen clearance on the long-term perspective, including stronger IFNγ production by T cells, which
434 indicates a long-lasting effect of the transient anti-IL-7/IL-7R administration at the peak of infection.
435 To specify the critical source of IL-7 mediating an immunosuppressing effect, we employed a
436 conditional *Il7* knockout mediated by *Prrx-cre*, which is active in the majority of skin fibroblasts around

437 birth (Leavitt et al., 2020; Liu et al., 2022), and is upregulated during wound healing (Lee et al., 2022).
438 Importantly, we show that *Il7* expression is affected by the conditional knockout only in fibroblasts, but
439 not any other stromal cell population sorted from the skin. The finding that *Prrx-cre* mediated *Il7* was
440 sufficient to enhance *L. major* clearance and effector $CD4^+$ T cell function therefore suggests that
441 fibroblasts are critical producers of IL-7 in the mechanism. Skin fibroblasts have been shown to increase
442 *Il7* expression in response to inflammation in a variety of models, including the infection of the ear
443 dermis with *L. major* (Peduto et al., 2009), which we could confirm. IFNγ, which we could show to be
444 mainly produced by T cells in our system, is sufficient to induce *Il7* expression upon injection in the
445 skin of uninfected mice. Conversely, anti-IFNγ injection decreases *Il7* expression in a model of
446 autoimmune alopecia (Dai et al., 2021). Therefore, it is conceivable that IFNγ produced by *L. major*-
447 specific T cells (Muller et al., 2012) initiates an IL-7 mediated feedback from fibroblasts which
448 ultimately dampens pathogen clearance. This mechanism might constitute a feedback switch that
449 activates immunosuppressive monocyte-derived cells as soon as local IFNγ production in the course of
450 the T cell response exceeds a certain threshold.
451 Targeting immunoregulatory mechanisms carries the risk of inducing immune-related adverse events
452 (Yan et al., 2024), including pathological effects of unrestricted T cell functions (Byrne and Fisher,
453 2017; Johnson et al., 2016; Murakami et al., 2016). Of note, we did only observe a slight, transient
454 increase of inflammation, while pathogen control was long-lasting. Two explanations are likely for this
455 finding: First, efficient pathogen control could decrease pathogen burden-dependent inflammation
456 (Formaglio et al., 2021), thereby masking the increased immune activation related to impaired IL-7
457 signaling. Second, the effector molecule nitric oxide, which is likely produced at higher amounts in
458 response to the increased IFNγ, can restrict leukocyte recruitment (Mishra et al., 2013; Postat et al.,
459 2018), thus counteracting an even more severe pathology in the anti-IL-7/IL-7R treated animals.
460 Therefore, targeting IL-7 mediated immunosuppression might be especially well-suited for enhancing
461 immune reactions involving nitric oxide-mediated killing by monocyte-derived cells, as nitric oxide
462 seems to provide an additional layer of immunoregulation. Such monocyte-mediated killing has been
463 demonstrated not only in immunity against intracellular pathogens (Olekhnovitch et al., 2014), but also
464 during T cell therapy against cancer (Kruse et al., 2023).

465 Taken together, we describe a cytokine-dependent feedback loop that can restrict T cell activation in
466 response to excessive IFNγ production, a mechanism from which the pathogen can benefit to perpetuate
467 the infection. Targeting this mechanism to adjust the activation of effector T cell functions opens new
468 avenues for future immunotherapeutic approaches.
469

470 **Methods**

471

472 *Ethics Statement*

473 All animal experiments were reviewed and approved by the Ethics Committee of the Office for
474 Veterinary Affairs of the State of Saxony-Anhalt, Germany (permit license numbers 42502-2-1314 UNI
475 MD, 42502-2-1393 Uni MD, 42502-2-1575 Uni MD, 42502-2-1586 Uni MD, 42502-2-1615 Uni MD,
476 42502-2-1672 Uni MD, and 42502-2-1735 Uni MD) in accordance with the legislation of both the
477 European Union (Council Directive 499 2010/63/EU) and the Federal Republic of Germany (according
478 to § 8, Section 1 TierSchG, and TierSchVersV).

479

480 *Parasites, tumor and mouse infections*

481 *L. major* LRC-L137 V121 wild-type, DsRed-, and mKikume-expressing (Lm^{SWITCH}) parasites were
482 described previously (Muller et al., 2013; Sorensen et al., 2003). *L. major* expressing the cyan
483 fluorescent protein mTurquoise ($Lm^{\mathrm{Turquoise}}$) was generated by targeted integration of the mTurquoise
484 gene into the recombinant RNA locus of L. major LRC-L137 V121. For this, the mTurquoise gene
485 (Goedhart et al., 2010) sequence was synthesized *de novo* (Eurofins Scientific) and cloned via BamHI-
486 BglII and NotI (New England Biolabs) into a pLEXSY-Hyg2 vector (Jena Bioscience). The resulting
487 plasmid was linearized usin SwaI (New England Biolabs) and electroporated into *L. major*. Stable
488 transfectants were selected with 30 mg/ml hygromycin B (Invitrogen). Single clones were obtained by
489 limiting dilution. All parasites were grown in M119 medium completed with 10% heat-inactivated fetal
490 calf serum, 0.1 mM adenine, 1 mg/ml biotin, 5 mg/ml hemin, and 2 mg/ml biopterin (all from Sigma)
491 and kept for a maximum of six passages.

492 Wild-type C57BL/6J and CD45.1 (B6.SJL-$Ptprc^{a}Pepc^{b}$/BoyJ, JAX stock #002014) mice, $Il7r^{-/-}$
493 (B6.129S7-$Il7r^{tm1Imx}$/J, JAX stock #002295,) (Peschon et al., 1994), $Rag1^{-/-}$ (B6.129S7-$Rag1^{tm1Mom}$/J,
494 JAX stock #002096) (Mombaerts et al., 1992), and mKikumeGR (Tg(CAG-KikGR)33Hadj/J, JAX
495 stock #013753) (Nowotschin and Hadjantonakis, 2009) mice were purchased from The Jackson
496 Laboratory (Bar Harbor, ME) via Charles River (Sulzfeld, Germany). Bone marrow from Ccr2-creERT2
497 (C57BL/6NTac-$Ccr2^{tm2982(T2A\text{-}Cre7ESR1\text{-}T2A\text{-}mKate2)BB}$) (Croxford et al., 2015) x Ai14(B6.Cg-

498 *Gt(ROSA)26Sor*$^{tm14(CAG\text{-}tdTomato)Hze}$) (Madisen et al., 2010) mice was provided by Melanie Greter and
499 Burkhard Becher (University of Zürich, Switzerland). To obtain *Prrx-cre* × *Il7*$^{fl/fl}$ animals, *Prrx-cre*
500 (B6.Cg-Tg(Prrx1-cre)1Cjt/J, JAX stock #005584) (Logan et al., 2002) mice were purchased from The
501 Jackson Laboratory and crossed to mice harboring floxed *Il7* alleles (*Il7*^{fl}*Il7*^{fl}), which had been
502 previously generated by removing a FRT flanked part of a "knockout-first" construct *Il7*$^{tm1a(EUCOMM)Wtsi}$
503 (provided by The European Conditional Mouse Mutagenesis Program (EUCOMM)) using a Flpo-
504 transgenic (Kranz et al., 2010) cross (Knop et al., 2020). To obtain *Pdpn-cre* × *Il7r*$^{fl/fl}$ and *Pdpn-cre* ×
505 iDTR animals, the sperm of Pdpn-cre mice (C57BL/6N-Tg(Pdpn-icre)14Biat/Biat, EM#11673) (Onder
506 et al., 2011) were purchased from European Mouse Mutant Archive (EMMA) and used in artificial
507 insemination procedures with *Il7r*$^{fl/fl}$ (Il7rtm1.1Asin/J, JAX stock #022143) (McCaughtry et al., 2012)
508 females and ROSA26iDTR (CBy.B6-Gt(ROSA)26Sortm1(HBEGF)Awai/J) (Buch et al., 2005)
509 females, respectively. The animals were housed and bred under specific-pathogen-free conditions in the
510 central animal facility (ZTL) of the Medical Faculty at Otto-von-Guericke-Magdeburg.
511 For infection, 2x10^6 stationary phase promastigotes were washed and resuspended in PBS and
512 subsequently injected in 10 µl into the ear dermis. Where indicated, Tamoxifen (Sigma-Aldrich) was
513 dissolved in olive oil (Sigma-Aldrich) at a concentration of 20 mg/ml and administered by i.p. injection
514 (100 mg/kg) for five consecutive days, either five days before the infection, or between days 11 through
515 15 p.i. The mouse melanoma cell line HCmel12 had been originally established from a primary
516 melanoma in the Hgf-Cd4k^{R24C} mouse model by serial transplantation as described previously (Bald et
517 al., 2014; Kruse et al., 2023), and were cultured in complete Roswell Park Memorial Institute (RPMI)
518 medium consisting of RPMI 1640 medium (Life Technologies) supplemented with 10% foetal calf
519 serum (Biochrome), 2 mM L-glutamine, 10 mM non-essential amino acids, 1 mM HEPES (all from Life
520 Technologies), 20 µM 2-mercoptoethanol (Sigma), 100 IU ml−1 penicillin and 100 µg ml−1
521 streptomycin (Invitrogen) in a humidified incubator with 5% CO_2. For tumor inoculation, a total of
522 2x10^5 cells were injected intracutaneously (i.c.) into the shaved flanks of mice with a 30G (0.3x13 mm)
523 injection needle (BD). Tumor development was monitored by inspection and palpation. Mice were
524 euthanized at 21 days post-tumor injection or before if tumors exceeded 15 mm mean diameter or when
525 mice showed signs of sickness in adherence with the local ethical regulations.

526

527 *Antibody treatment*

528 For anti-IL-7/IL-7R application, mice were intraperitoneally (i.p.) injected with 500 µg of anti-mouse
529 IL-7Rα (clone A7R34, Bio X Cell), which is non-depleting (Mai et al., 2014; Seddon et al., 2003), and
530 500 µg of anti-mouse IL7 (clone M25, Bio X Cell) per treatment (Table S6). Control mice were i.p.
531 injected with 500 µg of rat IgG2a isotype control (clone 2A3, Bio X Cell) and 500 µg of mouse IgG2b
532 isotype control (clone MPC-11, Bio X Cell) per treatment. For anti-IFNγ application, mice were i.p.
533 injected with 500 µg of anti-mouse IFNγ (clone R4-6A2, Bio X Cell) per treatment, while control mice
534 received 500 µg of rat IgG1 isotype control (clone HRPN, Bio X Cell) per treatment.

535

536 *Adoptive T cell and BM transfer, irradiation and BM chimera generation*

537 For adoptive transfer, $CD4^+$ T cells were isolated from axillary, brachial, cervical, and inguinal lymph
538 nodes as well as from the spleen using the CD4 isolation kit and negative selection MACS purification
539 (Miltenyi Biotech, Bergisch Gladbach, Germany) according to the manufacturer's instructions. 1×10^7
540 T cells per recipient were injected intravenously. For BM isolation, BM cells were flushed from tibia
541 and femur with ice-cold non-supplemented RPMI 1640 (PAN Biotec) and filtered through 100 micron
542 cell strainers. Cells were washed with non-supplemented PBS, and 4×10^7 cells (for BM reconstitution)
543 per recipient were resuspended in PBS and injected intravenously into the tail vein. For generating BM
544 chimeras or fully BM reconstituted mice, recipients were γ-irradiated with 9.5 gray before reconstitution
545 and infected 8 weeks later.

546

547 *Photoconversion for proliferation measurement and optical time-stamping*

548 Photoconversion of Lm^{SWITCH} parasites and cells in the mouse ear was performed with a 405 nm
549 wavelength, 665 mW/cm2 collimated high-power LED (Thorlabs). The ears of anesthetized mice were
550 fixed and illuminated from each side for 30 seconds at a distance of 20 cm and were analyzed after 48h
551 by flow cytometry.

552

553 *Flow cytometry*

554 Cells were harvested from digested ears as previously described (Heyde et al., 2018). Draining lymph
555 nodes or spleen were dissociated on a 70 µm cell strainer, and cells were washed with PBS. Surface
556 staining of cells was done by using the antibodies specified in table S6. For intracellular staining of IL-
557 1 beta (Pro-form), IL-6, IL-12 p35, CXCL9, Eomes, Foxp3, GATA3, RORgt, T-bet and IFNγ, the cell
558 suspension was fixed for 1hr at 4°C with fixation buffer (Biolegend), following permeabilization with
559 Perm/Wash solution (Biolegend) according to the manufacturer's instructions and stained with the
560 antibodies listed in table S6 prior to staining and analyzed on a Fortessa flow cytometer (BD
561 Biosciences). Samples with a content of less than 40% of CD11c-expressing cells among $CD45^+$ were
562 excluded from quantitative analysis. The mKikume fluorescence with/without photoconversion was
563 read out at 561 nm excitation and 610/20 nm emission, or 488 nm excitation and 530/30 nm emission,
564 respectively. An autofluorescence signal was recorded at 488 excitation and 695/40 nm emission. Data
565 were analyzed using the FlowJo software (FlowJo, LLC). qPCR of sorted cells was performed as
566 described in the supplemental materials and methods.
567
568 *Single-cell index sorting and SmartSeq2 sequencing library preparation*
569 For scRNAseq, mouse CD45 MicroBeads (Miltenyi Biotec) were used to isolate leukocytes prior to cell
570 surface staining according to manufacturer's instructions. In order to review the complete phenotype of
571 every single cell and associate every phenotype with each sorted single cell, index sorting was performed
572 on FACS ARIA III sorter (BD Biosciences). Single cells were sorted into different wells from a 96-well
573 plate (Costar) filled with 4.65 µl of Buffer RLT Plus (Qiagen), 0.25 µl of SUPERase-In RNase-Inhibitor
574 (Invitrogen), and 0.1 µl of ERCC spike-Mix1 (Invitrogen) pre-diluted 1:500000 in RNAse-free water.
575 For cell-population RNAseq, 50-100 cells per subpopulation per sample were sorted into the wells.
576 Sorted cells were immediately frozen and stored at -80 °C. Single-cell libraries were prepared using
577 Smart-seq2 protocol as previously described (Picelli et al., 2014) with minor modifications: Following
578 cDNA amplification, ACTB expression was measured in each cDNA library by qPCR. All cDNA
579 libraries were diluted aiming to an equivalent ct value for ACTB (average = 21.11, SD = 1.05) and were
580 subsequently used as input for a tagmentation-based protocol (Nextera XT, Illumina) using one quarter
581 of the recommended volumes, 10 min for tagmentation at 55°C (Saliba et al., 2016). Libraries were

582 quantified using Qubit dsDNA Hs Assay (Life Technologies) and fragment size of libraries was
583 analyzed using QIAxcel DNA high resolution Kit (Qiagen) and Bioanalyzer High Sensitivity DNA kit
584 (Agilent). Libraries were normalized to 2 nM and pooled. Particularly, 218 of single-cell libraries or 87
585 of cell-population libraries were sequenced for HiSeq PE200 (Illumina). Sequencing data was analysed
586 as described in the supplemental materials and methods.
587
588 *Processing of RNA sequencing data*
589 Raw fastq files were processed with Cutadapt (v3.7) (Martin, 2011) to remove poly-A tails and adapter
590 sequences from the SMART-seq and Nextera protocols. Low-quality bases (Q-score < 20) and reads left
591 with less than 25 bases after trimming were removed. Sequencing data were mapped to a reference
592 genome using STAR with default parameters (Dobin et al., 2013). The reference genome was built by
593 combining the mouse (GRCm38) and *Leishmania major* (ASM272v2) genomes as well as spike-ins
594 (ERCC92) and the Kikume Green-Red transcript sequences. Raw count matrices were generated from
595 the mapping results after read count quantification with featureCounts (Subread, v1.6.3) (Liao et al.,
596 2014). Two count matrices for 218 single cells and 87 cell-population libraries were created.
597
598 *Quality control and normalization of scRNAseq data*
599 Low-quality cells with more than 2% mitochondrial read counts, more than 20% ERCC spike-ins read
600 counts or less than 1000 detected genes were discarded. Only mouse genes with at least 5 read counts
601 detected in at least 10 cells were retained. Read counts for the 194 retained single-cell transcriptomes
602 were normalized with scNorm (Bacher et al., 2017). Information about the plate for technical biases
603 (*Condition*) and gene length (*WithinSample*) was considered during the normalization procedure.
604
605 *Dimensional reduction and clustering of scRNAseq data*
606 Downstream analysis of the single-cell dataset has been performed with the Seurat R package (v4.0)
607 (Hao et al., 2021). The normalized read count matrix was natural log-transformed and the top 1000
608 highly variables genes were identified (*FindVariableFeatures*). For dimensional reduction, principal
609 component analysis was performed (*RunPCA*) to capture the principal components (PCs) explaining the

610 highest amount of variation in the dataset. Batch effects between mice were corrected with Harmony
611 (v0.1.1). The top 8 PCs from the corrected PCA were projected into a 2D space by Uniform Manifold
612 Approximation Projection (*RunUMAP*) for data visualization. In the uncorrected data, we found that
613 cells from three infected ears were strongly separated from the rest of the cells by in UMAP 1 versus
614 UMAP 2 (see Fig. S1E). MACS-purified cells from these infected ears revealed a substantially lower
615 percentage of $CD11c^+$ cells than the remaining samples in other ears. While this war corrected for
616 scRNAseq, we excluded cells from samples with a $CD11c^+$ cell content of less than 40% from
617 experiments with functional readout.
618 A graph-based unsupervised machine learning procedure was used to identify groups of single cells with
619 similar transcriptomes, i.e. clusters. The top 8 PCs were used to build a KNN graph (*FindNeighbors*;
620 k = 10) followed by partition into clusters with the Leiden algorithm (Traag et al., 2019). We used the C
621 implementation for R of the Leiden algorithm (leidenbase v0.1.3, Trapnell Lab) with a resolution set at
622 0.08. Clustering results were used to label cells on the UMAP.
623
624 *Differential expression testing and pathway analysis for single-cell data*
625 Gene markers of each cluster were identified by a Wilcoxon Rank-Sum Test with Seurat
626 (*FindAllMarkers*). Only genes that were expressed in at least 10% of the cells from a given cluster, with
627 an absolute log2 fold-change > 0.25 and a Bonferroni adjusted p-value < 0.05 were considered as
628 differentially expressed.
629 Gene Set Enrichment Analysis (v4.3.2) was used for pathway analysis (Subramanian et al., 2005). DEG
630 testing was repeated over all genes by a Wilcoxon Rank-Sum Test for each cluster versus all others
631 through Seurat (*FindMarkers*). Gene-ranked lists were generated after converting all uncorrected p-
632 values to -log10(p-value) * fold-change direction. Ranked lists were used as input for GSEA preranked
633 with default parameters and Gene Ontology Biological Process gene sets. Pathways up- or down-
634 regulated with FDR < 0.05 were considered significant.
635
636 *Quantitative PCR analysis*

637 For validation of DEG identified in the scRNAseq, 50 cells per sample were sorted from each
638 subpopulation according to the gating strategy shown in fig. S1K and lysed in 10µl lysis buffer (RNeasy
639 Plus lysis buffer, QIAGEN) containing 5% SUPERase-In RNase-Inhibitor 20U/µl (Invitrogen). RNA
640 extraction and reverse transcription were performed using the Smart-seq2 protocol as previously
641 described (Picelli et al., 2014). Primers used are specified in table S6.
642 For measuring *Il7* gene expression, total RNA was isolated from *L. major*-infected ear tissue using
643 TRIzol reagent (Invitrogen) and then was reverse-transcribed using the High-Capacity cDNA Reverse
644 Transcription Kit (Applied Biosystems) following the manufacturer's instructions. In order to correct
645 for the immune cell infiltrate which was expected to contain leukocytes expressing *Hprt*, but not *Il7*)
646 *hprt* CT values were corrected according to the mean difference in RNA extracted.
647 For measuring the *Il7* and *Prrx1* gene expression in fibroblasts, LEC and BEC, three replicates of 200
648 cells each were sorted from each mouse ear. RNA extraction and reverse transcription was performed
649 using the Smart-Seq2 protocol as described above. Quantitative PCR analysis was done using a SYBR
650 Green Master Mix (Applied Biosystems).
651 To run the quantitative PCR, 40 cycles of 95 °C (15 s), and 60 °C (60 s) followed by a dissociation
652 protocol 95 °C (15 s), 60 °C (20 s), and 95 °C (15 s) were performed on an ABI Prism 7000 Sequence
653 detection system (Applied Biosystems). Technical triplicates were performed for each sample.
654
655
656 *Limiting dilution assay*
657 *L. major* burden within ear tissue was measured using a limiting dilution assay. Quadruplicate samples
658 of each ear homogenate were serially diluted in 1:2 steps in *Leishmania* culture medium in 96-well
659 plates and incubated at 26 °C for 14 days. The initial parasite burden was calculated from the median of
660 the highest dilutions of the quadruplicates which exhibited parasite growth. In order to compensate
661 experiment-to-experiment variation, the values were normalized to the control groups for pooled data.
662
663 *Proliferation analysis*

664 The proliferation index of *L. major* for flow cytometry was calculated based on the MFI of
665 mKikumeGreen and mKikumeRed as described previously (Heyde et al., 2018). In brief, for visualizing
666 qualitative comparisons within the same sample using the FlowJo software, values were plotted as

667 $$C - 100 * \left(\frac{mKikume\ Red}{mKikume\ Green}\right)_{\text{cell}} / \left(\frac{mKikume\ Red}{mKikume\ Green}\right)_{\text{mean (all infected cells)}}$$

668 with C chosen between 100 and 250 and kept constant within the same sample for which the comparison
669 was made, and the factor 100 was introduced to analyze integer fluorescence values in FlowJo.
670 For inter-sample comparison, the proliferation index was calculated as

671 $$1 - \left(\frac{mKikume\ Red}{mKikume\ Green}\right)_{\text{cell}} / \left(\frac{mKikume\ Red}{mKikume\ Green}\right)_{\text{mean (all infected cells)}}$$

672 and represented as a percent deviation from the total infected cell population within one sample or
673 imaged infection site.
674

675 *Cell culture and stimulation*

676 To generate a fibroblast culture, lymphoid stromal cells were isolated from peripheral lymph nodes of
677 C57BL/6J mice as described previously (Knop et al., 2020). Afterwards, cells from four mice were
678 pooled and seeded in a T25 flask in full medium (RPMI 1640 supplemented with 10% (v/v) FCS (FBS
679 Superior; Sigma) /1% (v/v) P/S (Gibco)/2 mM L-glutamine (Gibco)/1 mM sodium pyruvate (Gibco)/0.1
680 mM HEPES (Gibco)/50 µM 2-mercaptoethanol (Sigma). Cells were cultured for 24h at 37°C and 5%
681 CO_2 and non-attached cells were removed. When reaching confluence, cells were detached using
682 Trypsin/EDTA (Merck Biochrom) and seeded onto T75, and afterwards onto T175. Cells were detached
683 using Trypsin/EDTA and treated with biotinylated anti-CD45 (30-F11, Biolegend) and anti-CD31
684 (MEC13.3, Biolegend)-specific antibodies in degassed staining buffer (PBS/ 2 mM EDTA (Carl Roth)/
685 0,5% (w/v) BSA (AppliChem)) for 15min at 4°C. Cells were washed and resuspended in degassed PBS/
686 2 mM EDTA and CD45+ and CD31+ cells were depleted using Streptavidin MicroBeads (Miltenyi
687 Biotec), LS columns (Miltenyi Biotec) and MidiMACS separator (Miltenyi Biotec) according to
688 manufacturer's instructions. Cells were seeded in a T175 flask in full medium. When reaching
689 confluence, cells were detached using Accutase (Stempro, Gibco) and stained with anti-CD45.2-APC
690 (104, Biolegend), gp38-A488 (8.1.1, Biolegend) and CD31-PE/Cy7 (390, eBioscience)-specific

691 antibodies for 30min at 4°C in staining buffer containing purified anti-CD16/32 (2.4G2 ATCC® HB-
692 197TM). After washing with PBS/2 mM EDTA, cells were resuspended in full medium containing 2
693 µg/ml Ciprobay (Bayer) and $CD45.2^-$ $gp38^+CD31^-$ cells were sorted using FACSARIA III (Becton
694 Dickinson). The sorted cells were seeded at a density of 7400 cells/cm^2 in full medium containing 2
695 µg/ml Ciprobay. After 48h, Ciprobay was removed and the fibroblasts were expanded until reaching
696 confluence in a T175 flask.
697 For IFN-γ stimulation, cells were detached using Accutase and were seeded at 40000 cells/24-Well in
698 500 µl full medium without or with 50 ng/ml recombinant mouse IFN-γ (R&D Systems). After 24h, the
699 cells were detached using Accutase and resuspended in TRIzol reagent (Invitrogen). RNA isolation,
700 reverse transcription and RT-qPCR were performed as described previously (Knop et al., 2020). The
701 following TaqMan® Gene Expression Assays (Thermo Fisher Scientific) were used according to the
702 manufacturer's instructions: Il7 (FAM-MGB probe Mm01295804 m1) and Hprt (FAM-MGB probe
703 Mm00446968 m1). Each sample underwent analysis in triplicates on qTOWER3 G (Analytic Jena).
704 Subsequently, relative quantification was performed according to the ΔCT method.
705
706 *Re-analysis of published scRNAseq from tumor-associated monocyte-derived cells*
707 Unsupervised Leiden clustering and differential gene expression analysis for tumor-associated monocyt-
708 derived cells were obtained from our published data (Kruse et al., 2023) that had been deposited at the
709 NCBI GEO under the accession GSE230427 (raw data) and GSE230427 (normalized and logarithmized
710 count matrix). In brief, the data had been generated from individual tumors from which $CD45^+$ cells
711 were enriched using a positive selection kit (Miltenyi) and hashtagged with unique TotalSeq-B hashtag
712 antibodies B0301-B0310 (1:300, Biolegend) and subsequently stained with fluorescently labeled
713 antibodies. $CD45^+CD11b^+Ly6G^-$ cells were sorted with an Aria III fluorescence-activated cell sorter
714 (BD). Isolated cells were loaded onto one lane of a 10X Chromium microfluidics controller. Sequencing
715 was performed on an Illumina Novaseq on two lanes of a S1 cartridge with 150 bp read length in paired
716 end mode. Reading depth was calculated to obtain roughly 50,000 reads per cell for the gene expression
717 library and 5,000 reads per cell for the hashtag library. Monocytes and macrophages from non-treated
718 tumor clustered into T1 through T4 (Kruse et al., 2023) were re-analyzed regarding differential gene

719 expression between cells classified as Cluster T4 versus Cluster T1 through T3, and cells classified as
720 *Il7r*-expressing versus all other cells using a zero-inflated regression model from the R package MAST
721 (Finak et al., 2015).
722
723 *Statistical analysis*
724 Statistical analysis was carried out with GraphPad Prism 8 (GraphPad Software, San Diego, CA, USA).
725 To compare multiple samples in pairwise analysis within datasets with more than two experimental
726 groups, one-way analysis of variance (ANOVA) was done for datasets that had passed a Shapiro-Wilk
727 normal distribution test, Kruskal-Wallis tests were performed for datasets with non-normal distribution.
728 Appropriate multiple comparison post-tests (Bonferroni's for multiple comparisons, Dunnet's for
729 multiple pairwise comparisons or multiple comparisons with a control group in ANOVA, Dunn's test
730 for Kruskal-Wallis analyses) were employed as indicated in the respective figure legends. Two-group
731 comparisons were analyzed using two-sided, unpaired or paired t-tests for data with normal distribution
732 and Mann-Whitney tests for datasets for which a Shapiro-Wilk normal distribution suggested non-
733 normal distribution. Representation of the median or mean, with standard deviation in cases where not
734 all data points are shown individually, are indicated together with sample size in the figure legends.
735
736

737 **References**

738 Al-Mossawi, H., N. Yager, C.A. Taylor, E. Lau, S. Danielli, J. de Wit, J. Gilchrist, I. Nassiri, E.A.
739 Mahe, W. Lee, L. Rizvi, S. Makino, J. Cheeseman, M. Neville, J.C. Knight, P. Bowness, and B.P.
740 Fairfax. 2019. Context-specific regulation of surface and soluble IL7R expression by an
741 autoimmune risk allele. *Nat Commun* 10:4575.

742 Alexander, W.S., R. Starr, J.E. Fenner, C.L. Scott, E. Handman, N.S. Sprigg, J.E. Corbin, A.L.
743 Cornish, R. Darwiche, C.M. Owczarek, T.W. Kay, N.A. Nicola, P.J. Hertzog, D. Metcalf, and D.J.
744 Hilton. 1999. SOCS1 is a critical inhibitor of interferon gamma signaling and prevents the
745 potentially fatal neonatal actions of this cytokine. *Cell* 98:597-608.

746 Avraham, R., N. Haseley, D. Brown, C. Penaranda, H.B. Jijon, J.J. Trombetta, R. Satija, A.K. Shalek,
747 R.J. Xavier, A. Regev, and D.T. Hung. 2015. Pathogen Cell-to-Cell Variability Drives
748 Heterogeneity in Host Immune Responses. *Cell* 162:1309-1321.

749 Baasch, S., P. Giansanti, J. Kolter, A. Riedl, A.J. Forde, S. Runge, S. Zenke, R. Elling, A. Halenius, S.
750 Brabletz, H. Hengel, B. Kuster, T. Brabletz, L. Cicin-Sain, R. Arens, A. Vlachos, J.C. Rohr, M.P.
751 Stemmler, M. Kopf, Z. Ruzsics, and P. Henneke. 2021. Cytomegalovirus subverts macrophage
752 identity. *Cell* 184:3774-3793 e3725.

753 Bacher, R., L.F. Chu, N. Leng, A.P. Gasch, J.A. Thomson, R.M. Stewart, M. Newton, and C.
754 Kendziorski. 2017. SCnorm: robust normalization of single-cell RNA-seq data. *Nat Methods*
755 14:584-586.

756 Bachmann, M.F., P. Wolint, K. Schwarz, P. Jager, and A. Oxenius. 2005. Functional properties and
757 lineage relationship of CD8+ T cell subsets identified by expression of IL-7 receptor alpha and
758 CD62L. *J Immunol* 175:4686-4696.

759 Badovinac, V.P., S.E. Hamilton, and J.T. Harty. 2003. Viral infection results in massive CD8+ T cell
760 expansion and mortality in vaccinated perforin-deficient mice. *Immunity* 18:463-474.

761 Bald, T., T. Quast, J. Landsberg, M. Rogava, N. Glodde, D. Lopez-Ramos, J. Kohlmeyer, S.
762 Riesenberg, D. van den Boorn-Konijnenberg, C. Homig-Holzel, R. Reuten, B. Schadow, H.
763 Weighardt, D. Wenzel, I. Helfrich, D. Schadendorf, W. Bloch, M.E. Bianchi, C. Lugassy, R.L.
764 Barnhill, M. Koch, B.K. Fleischmann, I. Forster, W. Kastenmuller, W. Kolanus, M. Holzel, E.
765 Gaffal, and T. Tuting. 2014. Ultraviolet-radiation-induced inflammation promotes angiotropism
766 and metastasis in melanoma. *Nature* 507:109-113.

767 Bryson, B.D., T.R. Rosebrock, F.G. Tafesse, C.Y. Itoh, A. Nibasumba, G.H. Babunovic, B. Corleis, C.
768 Martin, C. Keegan, P. Andrade, S. Realegeno, D. Kwon, R.L. Modlin, and S.M. Fortune. 2019.
769 Heterogeneous GM-CSF signaling in macrophages is associated with control of Mycobacterium
770 tuberculosis. *Nat Commun* 10:2329.

771 Buch, T., F.L. Heppner, C. Tertilt, T.J. Heinen, M. Kremer, F.T. Wunderlich, S. Jung, and A.
772 Waisman. 2005. A Cre-inducible diphtheria toxin receptor mediates cell lineage ablation after toxin
773 administration. *Nat Methods* 2:419-426.

774 Byrne, E.H., and D.E. Fisher. 2017. Immune and molecular correlates in melanoma treated with
775 immune checkpoint blockade. *Cancer* 123:2143-2153.

776 Capitini, C.M., A.A. Chisti, and C.L. Mackall. 2009. Modulating T-cell homeostasis with IL-7:
777 preclinical and clinical studies. *J Intern Med* 266:141-153.

778 Carneiro, M.B., M.E. Lopes, L.S. Hohman, A. Romano, B.A. David, R. Kratofil, P. Kubes, M.L.
779 Workentine, A.C. Campos, L.Q. Vieira, and N.C. Peters. 2020. Th1-Th2 Cross-Regulation
780 Controls Early Leishmania Infection in the Skin by Modulating the Size of the Permissive
781 Monocytic Host Cell Reservoir. *Cell Host Microbe* 27:752-768 e757.

782 Carvalho, A., I.A. Ferraz, N.S. Hojo-Souza, F.A.C. Medeiros, L.A. Viana, D.C. Bartholomeu, A.T.
783 Chaves, T.M. de Souza, E.S.M.F. Costa, T.A.O. Mendes, M.C. Duarte, M. Rocha, and D.
784 Menezes-Souza. 2023. Chagas cardiomyopathy is associated with a high susceptibility to T. cruzi

785 infection in monocyte-derived macrophages and a predominance of CD4(+)CD45RO(+) T-cells
786 with immunoregulatory patterns. *Acta Trop* 237:106749.

787 Channappanavar, R., A.R. Fehr, R. Vijay, M. Mack, J. Zhao, D.K. Meyerholz, and S. Perlman. 2016.
788 Dysregulated Type I Interferon and Inflammatory Monocyte-Macrophage Responses Cause Lethal
789 Pneumonia in SARS-CoV-Infected Mice. *Cell Host Microbe* 19:181-193.

790 Cheng, S., Z. Li, R. Gao, B. Xing, Y. Gao, Y. Yang, S. Qin, L. Zhang, H. Ouyang, P. Du, L. Jiang, B.
791 Zhang, Y. Yang, X. Wang, X. Ren, J.X. Bei, X. Hu, Z. Bu, J. Ji, and Z. Zhang. 2021. A pan-cancer
792 single-cell transcriptional atlas of tumor infiltrating myeloid cells. *Cell* 184:792-809 e723.

793 Collins-McMillen, D., E.V. Stevenson, J.H. Kim, B.J. Lee, S.J. Cieply, M.T. Nogalski, G.C. Chan,
794 R.W. Frost, 3rd, C.R. Spohn, and A.D. Yurochko. 2017. Human Cytomegalovirus Utilizes a
795 Nontraditional Signal Transducer and Activator of Transcription 1 Activation Cascade via
796 Signaling through Epidermal Growth Factor Receptor and Integrins To Efficiently Promote the
797 Motility, Differentiation, and Polarization of Infected Monocytes. *J Virol* 91:

798 Colpitts, S.L., N.M. Dalton, and P. Scott. 2009. IL-7 receptor expression provides the potential for
799 long-term survival of both CD62Lhigh central memory T cells and Th1 effector cells during
800 Leishmania major infection. *J Immunol* 182:5702-5711.

801 Cool, T., A. Worthington, D. Poscablo, A. Hussaini, and E.C. Forsberg. 2020. Interleukin 7 receptor is
802 required for myeloid cell homeostasis and reconstitution by hematopoietic stem cells. *Exp Hematol*
803 90:39-45 e33.

804 Croxford, A.L., M. Lanzinger, F.J. Hartmann, B. Schreiner, F. Mair, P. Pelczar, B.E. Clausen, S. Jung,
805 M. Greter, and B. Becher. 2015. The Cytokine GM-CSF Drives the Inflammatory Signature of
806 CCR2+ Monocytes and Licenses Autoimmunity. *Immunity* 43:502-514.

807 Dai, Z., E.H.C. Wang, L. Petukhova, Y. Chang, E.Y. Lee, and A.M. Christiano. 2021. Blockade of IL-
808 7 signaling suppresses inflammatory responses and reverses alopecia areata in C3H/HeJ mice. *Sci*
809 *Adv* 7:

810 De Trez, C., S. Magez, S. Akira, B. Ryffel, Y. Carlier, and E. Muraille. 2009. iNOS-producing
811 inflammatory dendritic cells constitute the major infected cell type during the chronic Leishmania
812 major infection phase of C57BL/6 resistant mice. *PLoS Pathog* 5:e1000494.

813 Dobin, A., C.A. Davis, F. Schlesinger, J. Drenkow, C. Zaleski, S. Jha, P. Batut, M. Chaisson, and T.R.
814 Gingeras. 2013. STAR: ultrafast universal RNA-seq aligner. *Bioinformatics* 29:15-21.

815 Dolgachev, V.A., B. Yu, L. Sun, T.P. Shanley, K. Raghavendran, and M.R. Hemmila. 2014.
816 Interleukin 10 overexpression alters survival in the setting of gram-negative pneumonia following
817 lung contusion. *Shock* 41:301-310.

818 Dorhoi, A., V. Yeremeev, G. Nouailles, J. Weiner, 3rd, S. Jorg, E. Heinemann, D. Oberbeck-Muller,
819 J.K. Knaul, A. Vogelzang, S.T. Reece, K. Hahnke, H.J. Mollenkopf, V. Brinkmann, and S.H.
820 Kaufmann. 2014. Type I IFN signaling triggers immunopathology in tuberculosis-susceptible mice
821 by modulating lung phagocyte dynamics. *Eur J Immunol* 44:2380-2393.

822 Drewry, L.L., N.G. Jones, Q. Wang, M.D. Onken, M.J. Miller, and L.D. Sibley. 2019. The secreted
823 kinase ROP17 promotes Toxoplasma gondii dissemination by hijacking monocyte tissue migration.
824 *Nat Microbiol* 4:1951-1963.

825 Ellis, G.I., N.C. Sheppard, and J.L. Riley. 2021. Genetic engineering of T cells for immunotherapy.
826 *Nat Rev Genet* 22:427-447.

827 Evren, E., E. Ringqvist, K.P. Tripathi, N. Sleiers, I.C. Rives, A. Alisjahbana, Y. Gao, D. Sarhan, T.
828 Halle, C. Sorini, R. Lepzien, N. Marquardt, J. Michaelsson, A. Smed-Sorensen, J. Botling, M.C.I.
829 Karlsson, E.J. Villablanca, and T. Willinger. 2021. Distinct developmental pathways from blood
830 monocytes generate human lung macrophage diversity. *Immunity* 54:259-275 e257.

831 Finak, G., A. McDavid, M. Yajima, J. Deng, V. Gersuk, A.K. Shalek, C.K. Slichter, H.W. Miller, M.J.
832 McElrath, M. Prlic, P.S. Linsley, and R. Gottardo. 2015. MAST: a flexible statistical framework

833 for assessing transcriptional changes and characterizing heterogeneity in single-cell RNA
834 sequencing data. *Genome Biol* 16:278.

835 Formaglio, P., M. Alabdullah, A. Siokis, J. Handschuh, I. Sauerland, Y. Fu, A. Krone, P. Gintschel, J.
836 Stettin, S. Heyde, J. Mohr, L. Philipsen, A. Schroder, P.A. Robert, G. Zhao, S. Khailaie, A.
837 Dudeck, J. Bertrand, G.F. Spath, S. Kahlfuss, P. Bousso, B. Schraven, J. Huehn, S. Binder, M.
838 Meyer-Hermann, and A.J. Muller. 2021. Nitric oxide controls proliferation of Leishmania major by
839 inhibiting the recruitment of permissive host cells. *Immunity* 54:2724-2739 e2710.

840 Fry, T.J., and C.L. Mackall. 2002. Interleukin-7: from bench to clinic. *Blood* 99:3892-3904.

841 Gessner, A., A. Will, M. Vieth, K. Schroppel, and M. Rollinghoff. 1995. Stimulation of B-cell
842 lymphopoiesis by interleukin-7 leads to aggravation of murine leishmaniasis. *Immunology* 84:416-
843 422.

844 Gocher, A.M., C.J. Workman, and D.A.A. Vignali. 2022. Interferon-gamma: teammate or opponent in
845 the tumour microenvironment? *Nat Rev Immunol* 22:158-172.

846 Goedhart, J., L. van Weeren, M.A. Hink, N.O. Vischer, K. Jalink, and T.W. Gadella, Jr. 2010. Bright
847 cyan fluorescent protein variants identified by fluorescence lifetime screening. *Nat Methods* 7:137-
848 139.

849 Grabstein, K.H., T.J. Waldschmidt, F.D. Finkelman, B.W. Hess, A.R. Alpert, N.E. Boiani, A.E.
850 Namen, and P.J. Morrissey. 1993. Inhibition of murine B and T lymphopoiesis in vivo by an anti-
851 interleukin 7 monoclonal antibody. *J Exp Med* 178:257-264.

852 Guilliams, M., A. Mildner, and S. Yona. 2018. Developmental and Functional Heterogeneity of
853 Monocytes. *Immunity* 49:595-613.

854 Gundra, U.M., N.M. Girgis, M.A. Gonzalez, M. San Tang, H.J.P. Van Der Zande, J.D. Lin, M.
855 Ouimet, L.J. Ma, J. Poles, N. Vozhilla, E.A. Fisher, K.J. Moore, and P. Loke. 2017. Vitamin A
856 mediates conversion of monocyte-derived macrophages into tissue-resident macrophages during
857 alternative activation. *Nat Immunol* 18:642-653.

858 Gundra, U.M., N.M. Girgis, D. Ruckerl, S. Jenkins, L.N. Ward, Z.D. Kurtz, K.E. Wiens, M.S. Tang,
859 U. Basu-Roy, A. Mansukhani, J.E. Allen, and P. Loke. 2014. Alternatively activated macrophages
860 derived from monocytes and tissue macrophages are phenotypically and functionally distinct.
861 *Blood* 123:e110-122.

862 Hao, Y., S. Hao, E. Andersen-Nissen, W.M. Mauck, 3rd, S. Zheng, A. Butler, M.J. Lee, A.J. Wilk, C.
863 Darby, M. Zager, P. Hoffman, M. Stoeckius, E. Papalexi, E.P. Mimitou, J. Jain, A. Srivastava, T.
864 Stuart, L.M. Fleming, B. Yeung, A.J. Rogers, J.M. McElrath, C.A. Blish, R. Gottardo, P. Smibert,
865 and R. Satija. 2021. Integrated analysis of multimodal single-cell data. *Cell* 184:3573-3587 e3529.

866 Hara, T., S. Shitara, K. Imai, H. Miyachi, S. Kitano, H. Yao, S. Tani-ichi, and K. Ikuta. 2012.
867 Identification of IL-7-producing cells in primary and secondary lymphoid organs using IL-7-GFP
868 knock-in mice. *J Immunol* 189:1577-1584.

869 Harelimana, J.D., H.S. Ahor, B. Benner, S. Hellmuth, E. Adankwah, D. Minadzi, W. Aniagyei,
870 M.N.K. Lamptey, J. Arthur, A. Yeboah, M.K. Abass, L.B. Debrah, D.O. Owusu, E. Mayatepek, J.
871 Seyfarth, R.O. Phillips, and M. Jacobsen. 2022. Cytokine-induced transient monocyte IL-7Ra
872 expression and the serum milieu in tuberculosis. *Eur J Immunol* 52:958-969.

873 Heyde, S., L. Philipsen, P. Formaglio, Y. Fu, I. Baars, G. Hobbel, C.L. Kleinholz, E.A. Seiss, J.
874 Stettin, P. Gintschel, A. Dudeck, P. Bousso, B. Schraven, and A.J. Muller. 2018. CD11c-expressing
875 Ly6C+CCR2+ monocytes constitute a reservoir for efficient Leishmania proliferation and cell-to-
876 cell transmission. *PLoS Pathog* 14:e1007374.

877 Hoffman, D., Y. Tevet, S. Trzebanski, G. Rosenberg, L. Vainman, A. Solomon, S. Hen-Avivi, N.B.
878 Ben-Moshe, and R. Avraham. 2021. A non-classical monocyte-derived macrophage subset
879 provides a splenic replication niche for intracellular Salmonella. *Immunity* 54:2712-2723 e2716.

880 Hoffmann, C., F. Noel, M. Grandclaudon, L. Massenet-Regad, P. Michea, P. Sirven, L. Faucheux, A.
881 Surun, O. Lantz, M. Bohec, J. Ye, W. Guo, J. Rochefort, J. Klijanienko, S. Baulande, C. Lecerf, M.

882 Kamal, C. Le Tourneau, M. Guillot-Delost, and V. Soumelis. 2022. PD-L1 and ICOSL
883 discriminate human Secretory and Helper dendritic cells in cancer, allergy and autoimmunity. *Nat*
884 *Commun* 13:1983.

885 Hou, T.Z., J. Bystrom, J.P. Sherlock, O. Qureshi, S.M. Parnell, G. Anderson, D.W. Gilroy, and C.D.
886 Buckley. 2010. A distinct subset of podoplanin (gp38) expressing F4/80+ macrophages mediate
887 phagocytosis and are induced following zymosan peritonitis. *FEBS Lett* 584:3955-3961.

888 Hovd, A.K., S. Nayar, C.G. Smith, P. Kanapathippillai, V. Iannizzotto, F. Barone, K.A. Fenton, and
889 H.L. Pedersen. 2024. Podoplanin expressing macrophages and their involvement in tertiary
890 lymphoid structures in mouse models of Sjogren's disease. *Front Immunol* 15:1455238.

891 Hu, X., A.Y. Chung, I. Wu, J. Foldi, J. Chen, J.D. Ji, T. Tateya, Y.J. Kang, J. Han, M. Gessler, R.
892 Kageyama, and L.B. Ivashkiv. 2008. Integrated regulation of Toll-like receptor responses by Notch
893 and interferon-gamma pathways. *Immunity* 29:691-703.

894 Huster, K.M., V. Busch, M. Schiemann, K. Linkemann, K.M. Kerksiek, H. Wagner, and D.H. Busch.
895 2004. Selective expression of IL-7 receptor on memory T cells identifies early CD40L-dependent
896 generation of distinct CD8+ memory T cell subsets. *Proc Natl Acad Sci U S A* 101:5610-5615.

897 Janson, P.C., P. Marits, M. Thorn, R. Ohlsson, and O. Winqvist. 2008. CpG methylation of the IFNG
898 gene as a mechanism to induce immunosuppression [correction of immunosupression] in tumor-
899 infiltrating lymphocytes. *J Immunol* 181:2878-2886.

900 Johnson, D.B., J.M. Balko, M.L. Compton, S. Chalkias, J. Gorham, Y. Xu, M. Hicks, I. Puzanov,
901 M.R. Alexander, T.L. Bloomer, J.R. Becker, D.A. Slosky, E.J. Phillips, M.A. Pilkinton, L. Craig-
902 Owens, N. Kola, G. Plautz, D.S. Reshef, J.S. Deutsch, R.P. Deering, B.A. Olenchock, A.H.
903 Lichtman, D.M. Roden, C.E. Seidman, I.J. Koralnik, J.G. Seidman, R.D. Hoffman, J.M. Taube,
904 L.A. Diaz, Jr., R.A. Anders, J.A. Sosman, and J.J. Moslehi. 2016. Fulminant Myocarditis with
905 Combination Immune Checkpoint Blockade. *N Engl J Med* 375:1749-1755.

906 Kaech, S.M., J.T. Tan, E.J. Wherry, B.T. Konieczny, C.D. Surh, and R. Ahmed. 2003. Selective
907 expression of the interleukin 7 receptor identifies effector CD8 T cells that give rise to long-lived
908 memory cells. *Nat Immunol* 4:1191-1198.

909 Kerrigan, A.M., L. Navarro-Nunez, E. Pyz, B.A. Finney, J.A. Willment, S.P. Watson, and G.D.
910 Brown. 2012. Podoplanin-expressing inflammatory macrophages activate murine platelets via
911 CLEC-2. *J Thromb Haemost* 10:484-486.

912 Knop, L., K. Deiser, U. Bank, A. Witte, J. Mohr, L. Philipsen, H.J. Fehling, A.J. Muller, U. Kalinke,
913 and T. Schuler. 2020. IL-7 derived from lymph node fibroblastic reticular cells is dispensable for
914 naive T cell homeostasis but crucial for central memory T cell survival. *Eur J Immunol* 50:846-
915 857.

916 Kranz, A., J. Fu, K. Duerschke, S. Weidlich, R. Naumann, A.F. Stewart, and K. Anastassiadis. 2010.
917 An improved Flp deleter mouse in C57Bl/6 based on Flpo recombinase. *Genesis* 48:512-520.

918 Kruse, B., A.C. Buzzai, N. Shridhar, A.D. Braun, S. Gellert, K. Knauth, J. Pozniak, J. Peters, P.
919 Dittmann, M. Mengoni, T.C. van der Sluis, S. Hohn, A. Antoranz, A. Krone, Y. Fu, D. Yu, M.
920 Essand, R. Geffers, D. Mougiakakos, S. Kahlfuss, H. Kashkar, E. Gaffal, F.M. Bosisio, O. Bechter,
921 F. Rambow, J.C. Marine, W. Kastenmuller, A.J. Muller, and T. Tuting. 2023. CD4(+) T cell-
922 induced inflammatory cell death controls immune-evasive tumours. *Nature* 618:1033-1040.

923 Leavitt, T., M.S. Hu, M.R. Borrelli, M. Januszyk, J.T. Garcia, R.C. Ransom, S. Mascharak, H.E.
924 desJardins-Park, U.M. Litzenburger, G.G. Walmsley, C.D. Marshall, A.L. Moore, B. Duoto, S.
925 Adem, D.S. Foster, A. Salhotra, A.H. Shen, M. Griffin, E.Z. Shen, L.A. Barnes, E.R. Zielins, Z.N.
926 Maan, Y. Wei, C.K.F. Chan, D.C. Wan, H.P. Lorenz, H.Y. Chang, G.C. Gurtner, and M.T.
927 Longaker. 2020. Prrx1 Fibroblasts Represent a Pro-fibrotic Lineage in the Mouse Ventral Dermis.
928 *Cell Rep* 33:108356.

929 Lee, K.W., S.Y. Yeo, J.R. Gong, O.J. Koo, I. Sohn, W.Y. Lee, H.C. Kim, S.H. Yun, Y.B. Cho, M.A.
930 Choi, S. An, J. Kim, C.O. Sung, K.H. Cho, and S.H. Kim. 2022. PRRX1 is a master transcription
931 factor of stromal fibroblasts for myofibroblastic lineage progression. *Nat Commun* 13:2793.

932 Lee, S.H., M. Charmoy, A. Romano, A. Paun, M.M. Chaves, F.O. Cope, D.A. Ralph, and D.L. Sacks.
933 2018. Mannose receptor high, M2 dermal macrophages mediate nonhealing Leishmania major
934 infection in a Th1 immune environment. *J Exp Med* 215:357-375.

935 Lee, S.H., M.M. Chaves, O. Kamenyeva, P.H. Gazzinelli-Guimaraes, B. Kang, G. Pessenda, K.
936 Passelli, F. Tacchini-Cottier, J. Kabat, E.A. Jacobsen, T.B. Nutman, and D.L. Sacks. 2020. M2-
937 like, dermal macrophages are maintained via IL-4/CCL24-mediated cooperative interaction with
938 eosinophils in cutaneous leishmaniasis. *Sci Immunol* 5:

939 Lee, S.H., B. Kang, O. Kamenyeva, T.R. Ferreira, K. Cho, J.S. Khillan, J. Kabat, B.L. Kelsall, and
940 D.L. Sacks. 2023. Dermis resident macrophages orchestrate localized ILC2 eosinophil circuitries to
941 promote non-healing cutaneous leishmaniasis. *Nat Commun* 14:7852.

942 Leon, B., M. Lopez-Bravo, and C. Ardavin. 2007. Monocyte-derived dendritic cells formed at the
943 infection site control the induction of protective T helper 1 responses against Leishmania. *Immunity*
944 26:519-531.

945 Leung, G.A., T. Cool, C.H. Valencia, A. Worthington, A.E. Beaudin, and E.C. Forsberg. 2019. The
946 lymphoid-associated interleukin 7 receptor (IL7R) regulates tissue-resident macrophage
947 development. *Development* 146:

948 Liao, Y., G.K. Smyth, and W. Shi. 2014. featureCounts: an efficient general purpose program for
949 assigning sequence reads to genomic features. *Bioinformatics* 30:923-930.

950 Liu, H., P. Li, S. Zhang, J. Xiang, R. Yang, J. Liu, M. Shafiquzzaman, S. Biswas, Z. Wei, Z. Zhang,
951 X. Zhou, F. Yin, Y. Xie, S.P. Goff, L. Chen, and B. Li. 2022. Prrx1 marks stem cells for bone,
952 white adipose tissue and dermis in adult mice. *Nat Genet* 54:1946-1958.

953 Logan, M., J.F. Martin, A. Nagy, C. Lobe, E.N. Olson, and C.J. Tabin. 2002. Expression of Cre
954 Recombinase in the developing mouse limb bud driven by a Prxl enhancer. *Genesis* 33:77-80.

955 Madisen, L., T.A. Zwingman, S.M. Sunkin, S.W. Oh, H.A. Zariwala, H. Gu, L.L. Ng, R.D. Palmiter,
956 M.J. Hawrylycz, A.R. Jones, E.S. Lein, and H. Zeng. 2010. A robust and high-throughput Cre
957 reporting and characterization system for the whole mouse brain. *Nat Neurosci* 13:133-140.

958 Mai, H.L., F. Boeffard, J. Longis, R. Danger, B. Martinet, F. Haspot, B. Vanhove, S. Brouard, and J.P.
959 Soulillou. 2014. IL-7 receptor blockade following T cell depletion promotes long-term allograft
960 survival. *J Clin Invest* 124:1723-1733.

961 Mandell, M.A., and S.M. Beverley. 2017. Continual renewal and replication of persistent Leishmania
962 major parasites in concomitantly immune hosts. *Proc Natl Acad Sci U S A* 114:E801-E810.

963 Mantovani, A., P. Allavena, F. Marchesi, and C. Garlanda. 2022. Macrophages as tools and targets in
964 cancer therapy. *Nat Rev Drug Discov* 21:799-820.

965 Marine, J.C., D.J. Topham, C. McKay, D. Wang, E. Parganas, D. Stravopodis, A. Yoshimura, and J.N.
966 Ihle. 1999. SOCS1 deficiency causes a lymphocyte-dependent perinatal lethality. *Cell* 98:609-616.

967 Mariotti, S., R. Teloni, E. Iona, L. Fattorini, G. Romagnoli, M.C. Gagliardi, G. Orefici, and R. Nisini.
968 2004. Mycobacterium tuberculosis diverts alpha interferon-induced monocyte differentiation from
969 dendritic cells into immunoprivileged macrophage-like host cells. *Infect Immun* 72:4385-4392.

970 Martin, M. 2011. Cutadapt removes adapter sequences from high-throughput sequencing reads.
971 *EMBnet. journal* 17:10-12.

972 McCaughtry, T.M., R. Etzensperger, A. Alag, X. Tai, S. Kurtulus, J.H. Park, A. Grinberg, P. Love, L.
973 Feigenbaum, B. Erman, and A. Singer. 2012. Conditional deletion of cytokine receptor chains
974 reveals that IL-7 and IL-15 specify CD8 cytotoxic lineage fate in the thymus. *J Exp Med* 209:2263-
975 2276.

976 Mishra, B.B., V.A. Rathinam, G.W. Martens, A.J. Martinot, H. Kornfeld, K.A. Fitzgerald, and C.M.
977 Sassetti. 2013. Nitric oxide controls the immunopathology of tuberculosis by inhibiting NLRP3
978 inflammasome-dependent processing of IL-1beta. *Nat Immunol* 14:52-60.

979 Mombaerts, P., J. Iacomini, R.S. Johnson, K. Herrup, S. Tonegawa, and V.E. Papaioannou. 1992.
980 RAG-1-deficient mice have no mature B and T lymphocytes. *Cell* 68:869-877.

981 Mulder, K., A.A. Patel, W.T. Kong, C. Piot, E. Halitzki, G. Dunsmore, S. Khalilnezhad, S.E. Irac, A.
982 Dubuisson, M. Chevrier, X.M. Zhang, J.K.C. Tam, T.K.H. Lim, R.M.M. Wong, R. Pai, A.I.S.
983 Khalil, P.K.H. Chow, S.Z. Wu, G. Al-Eryani, D. Roden, A. Swarbrick, J.K.Y. Chan, S. Albani, L.
984 Derosa, L. Zitvogel, A. Sharma, J. Chen, A. Silvin, A. Bertoletti, C. Bleriot, C.A. Dutertre, and F.
985 Ginhoux. 2021. Cross-tissue single-cell landscape of human monocytes and macrophages in health
986 and disease. *Immunity* 54:1883-1900 e1885.

987 Muller, A.J., S. Aeschlimann, R. Olekhnovitch, M. Dacher, G.F. Spath, and P. Bousso. 2013.
988 Photoconvertible pathogen labeling reveals nitric oxide control of Leishmania major infection in
989 vivo via dampening of parasite metabolism. *Cell Host Microbe* 14:460-467.

990 Muller, A.J., O. Filipe-Santos, G. Eberl, T. Aebischer, G.F. Spath, and P. Bousso. 2012. CD4+ T cells
991 rely on a cytokine gradient to control intracellular pathogens beyond sites of antigen presentation.
992 *Immunity* 37:147-157.

993 Murakami, N., T.J. Borges, M. Yamashita, and L.V. Riella. 2016. Severe acute interstitial nephritis
994 after combination immune-checkpoint inhibitor therapy for metastatic melanoma. *Clin Kidney J*
995 9:411-417.

996 Nalio Ramos, R., Y. Missolo-Koussou, Y. Gerber-Ferder, C.P. Bromley, M. Bugatti, N.G. Nunez, J.
997 Tosello Boari, W. Richer, L. Menger, J. Denizeau, C. Sedlik, P. Caudana, F. Kotsias, L.L.
998 Niborski, S. Viel, M. Bohec, S. Lameiras, S. Baulande, L. Lesage, A. Nicolas, D. Meseure, A.
999 Vincent-Salomon, F. Reyal, C.A. Dutertre, F. Ginhoux, L. Vimeux, E. Donnadieu, B. Buttard, J.
1000 Galon, S. Zelenay, W. Vermi, P. Guermonprez, E. Piaggio, and J. Helft. 2022. Tissue-resident
1001 FOLR2(+) macrophages associate with CD8(+) T cell infiltration in human breast cancer. *Cell*
1002 185:1189-1207 e1125.

1003 Navarro, S., G. Cossalter, C. Chiavaroli, A. Kanda, S. Fleury, A. Lazzari, J. Cazareth, T. Sparwasser,
1004 D. Dombrowicz, N. Glaichenhaus, and V. Julia. 2011. The oral administration of bacterial extracts
1005 prevents asthma via the recruitment of regulatory T cells to the airways. *Mucosal Immunol* 4:53-65.

1006 Nowotschin, S., and A.K. Hadjantonakis. 2009. Use of KikGR a photoconvertible green-to-red
1007 fluorescent protein for cell labeling and lineage analysis in ES cells and mouse embryos. *BMC Dev*
1008 *Biol* 9:49.

1009 Olekhnovitch, R., B. Ryffel, A.J. Muller, and P. Bousso. 2014. Collective nitric oxide production
1010 provides tissue-wide immunity during Leishmania infection. *J Clin Invest* 124:1711-1722.

1011 Onder, L., E. Scandella, Q. Chai, S. Firner, C.T. Mayer, T. Sparwasser, V. Thiel, T. Rulicke, and B.
1012 Ludewig. 2011. A novel bacterial artificial chromosome-transgenic podoplanin-cre mouse targets
1013 lymphoid organ stromal cells in vivo. *Front Immunol* 2:50.

1014 Ortega-Gomez, A., M. Perretti, and O. Soehnlein. 2013. Resolution of inflammation: an integrated
1015 view. *EMBO Mol Med* 5:661-674.

1016 Oyesola, O.O., K.L. Hilligan, S. Namasivayam, N. Howard, C.S. Clancy, M. Zhao, S.D. Oland, K.N.
1017 Kiwanuka, N.L. Garza, B.A.P. Lafont, R.F. Johnson, K.D. Mayer-Barber, A. Sher, and P. Loke.
1018 2023. Exposure to lung-migrating helminth protects against murine SARS-CoV-2 infection through
1019 macrophage-dependent T cell activation. *Sci Immunol* 8:eadf8161.

1020 Patir, A., A. Gossner, P. Ramachandran, J. Alves, T.C. Freeman, N.C. Henderson, M. Watson, and
1021 M.A. Hassan. 2020. Single-cell RNA-seq reveals CD16(-) monocytes as key regulators of human
1022 monocyte transcriptional response to Toxoplasma. *Sci Rep* 10:21047.

1023 Peduto, L., S. Dulauroy, M. Lochner, G.F. Spath, M.A. Morales, A. Cumano, and G. Eberl. 2009.
1024 Inflammation recapitulates the ontogeny of lymphoid stromal cells. *J Immunol* 182:5789-5799.

1025 Peschon, J.J., P.J. Morrissey, K.H. Grabstein, F.J. Ramsdell, E. Maraskovsky, B.C. Gliniak, L.S. Park,
1026 S.F. Ziegler, D.E. Williams, C.B. Ware, J.D. Meyer, and B.L. Davison. 1994. Early lymphocyte
1027 expansion is severely impaired in interleukin 7 receptor-deficient mice. *J Exp Med* 180:1955-1960.

1028 Picelli, S., A.K. Bjorklund, O.R. Faridani, S. Sagasser, G. Winberg, and R. Sandberg. 2013. Smart-
1029 seq2 for sensitive full-length transcriptome profiling in single cells. *Nat Methods* 10:1096-1098.

1030 Picelli, S., O.R. Faridani, A.K. Bjorklund, G. Winberg, S. Sagasser, and R. Sandberg. 2014. Full-
1031 length RNA-seq from single cells using Smart-seq2. *Nat Protoc* 9:171-181.

1032 Pisu, D., L. Huang, V. Narang, M. Theriault, G. Le-Bury, B. Lee, A.E. Lakudzala, D.T. Mzinza, D.V.
1033 Mhango, S.C. Mitini-Nkhoma, K.C. Jambo, A. Singhal, H.C. Mwandumba, and D.G. Russell.
1034 2021. Single cell analysis of M. tuberculosis phenotype and macrophage lineages in the infected
1035 lung. *J Exp Med* 218:

1036 Postat, J., R. Olekhnovitch, F. Lemaitre, and P. Bousso. 2018. A Metabolism-Based Quorum Sensing
1037 Mechanism Contributes to Termination of Inflammatory Responses. *Immunity* 49:654-665 e655.

1038 Rayes, J., S. Lax, S. Wichaiyo, S.K. Watson, Y. Di, S. Lombard, B. Grygielska, S.W. Smith, K.
1039 Skordilis, and S.P. Watson. 2017. The podoplanin-CLEC-2 axis inhibits inflammation in sepsis.
1040 *Nat Commun* 8:2239.

1041 Romano, A., M.B.H. Carneiro, N.A. Doria, E.H. Roma, F.L. Ribeiro-Gomes, E. Inbar, S.H. Lee, J.
1042 Mendez, A. Paun, D.L. Sacks, and N.C. Peters. 2017. Divergent roles for Ly6C+CCR2+CX3CR1+
1043 inflammatory monocytes during primary or secondary infection of the skin with the intra-
1044 phagosomal pathogen Leishmania major. *PLoS Pathog* 13:e1006479.

1045 Saliba, A.E., L. Li, A.J. Westermann, S. Appenzeller, D.A. Stapels, L.N. Schulte, S. Helaine, and J.
1046 Vogel. 2016. Single-cell RNA-seq ties macrophage polarization to growth rate of intracellular
1047 Salmonella. *Nat Microbiol* 2:16206.

1048 Sanin, D.E., Y. Ge, E. Marinkovic, A.M. Kabat, A. Castoldi, G. Caputa, K.M. Grzes, J.D. Curtis, E.A.
1049 Thompson, S. Willenborg, S. Dichtl, S. Reinhardt, A. Dahl, E.L. Pearce, S.A. Eming, A. Gerbaulet,
1050 A. Roers, P.J. Murray, and E.J. Pearce. 2022. A common framework of monocyte-derived
1051 macrophage activation. *Sci Immunol* 7:eabl7482.

1052 Seddon, B., P. Tomlinson, and R. Zamoyska. 2003. Interleukin 7 and T cell receptor signals regulate
1053 homeostasis of CD4 memory cells. *Nat Immunol* 4:680-686.

1054 Sorensen, M., C. Lippuner, T. Kaiser, A. Misslitz, T. Aebischer, and D. Bumann. 2003. Rapidly
1055 maturing red fluorescent protein variants with strongly enhanced brightness in bacteria. *FEBS Lett*
1056 552:110-114.

1057 Stapels, D.A.C., P.W.S. Hill, A.J. Westermann, R.A. Fisher, T.L. Thurston, A.E. Saliba, I.
1058 Blommestein, J. Vogel, and S. Helaine. 2018. Salmonella persisters undermine host immune
1059 defenses during antibiotic treatment. *Science* 362:1156-1160.

1060 Subramanian, A., P. Tamayo, V.K. Mootha, S. Mukherjee, B.L. Ebert, M.A. Gillette, A. Paulovich,
1061 S.L. Pomeroy, T.R. Golub, E.S. Lander, and J.P. Mesirov. 2005. Gene set enrichment analysis: a
1062 knowledge-based approach for interpreting genome-wide expression profiles. *Proc Natl Acad Sci U*
1063 *S A* 102:15545-15550.

1064 Sugimoto, M.A., L.P. Sousa, V. Pinho, M. Perretti, and M.M. Teixeira. 2016. Resolution of
1065 Inflammation: What Controls Its Onset? *Front Immunol* 7:160.

1066 Szabo, P.A., P. Dogra, J.I. Gray, S.B. Wells, T.J. Connors, S.P. Weisberg, I. Krupska, R. Matsumoto,
1067 M.M.L. Poon, E. Idzikowski, S.E. Morris, C. Pasin, A.J. Yates, A. Ku, M. Chait, J. Davis-Porada,
1068 X.V. Guo, J. Zhou, M. Steinle, S. Mackay, A. Saqi, M.R. Baldwin, P.A. Sims, and D.L. Farber.
1069 2021. Longitudinal profiling of respiratory and systemic immune responses reveals myeloid cell-
1070 driven lung inflammation in severe COVID-19. *Immunity* 54:797-814 e796.

1071 Traag, V.A., L. Waltman, and N.J. van Eck. 2019. From Louvain to Leiden: guaranteeing well-
1072 connected communities. *Sci Rep* 9:5233.

1073 Veglia, F., E. Sanseviero, and D.I. Gabrilovich. 2021. Myeloid-derived suppressor cells in the era of
1074 increasing myeloid cell diversity. *Nat Rev Immunol* 21:485-498.

1075 Wallis, R.S., A. O'Garra, A. Sher, and A. Wack. 2023. Host-directed immunotherapy of viral and
1076 bacterial infections: past, present and future. *Nat Rev Immunol* 23:121-133.

1077 Wolowczuk, I., M. Delacre, O. Roye, S.L. Giannini, and C. Auriault. 1997. Interleukin-7 in the skin of
1078 Schistosoma mansoni-infected mice is associated with a decrease in interferon-gamma production
1079 and leads to an aggravation of the disease. *Immunology* 91:35-44.

1080 Wykes, M.N., and S.R. Lewin. 2018. Immune checkpoint blockade in infectious diseases. *Nat Rev*
1081 *Immunol* 18:91-104.

1082 Xie, Z., B. Shao, C. Hoover, M. McDaniel, J. Song, M. Jiang, Z. Ma, F. Yang, J. Han, X. Bai, C.
1083 Ruan, and L. Xia. 2020. Monocyte upregulation of podoplanin during early sepsis induces
1084 complement inhibitor release to protect liver function. *JCI Insight* 5:

1085 Yamada, K.J., C.E. Heim, X. Xi, K.S. Attri, D. Wang, W. Zhang, P.K. Singh, T.K. Bronich, and T.
1086 Kielian. 2020. Monocyte metabolic reprogramming promotes pro-inflammatory activity and
1087 Staphylococcus aureus biofilm clearance. *PLoS Pathog* 16:e1008354.

1088 Yan, T., L. Yu, J. Zhang, Y. Chen, Y. Fu, J. Tang, and D. Liao. 2024. Achilles' Heel of currently
1089 approved immune checkpoint inhibitors: immune related adverse events. *Front Immunol*
1090 15:1292122.

1091 Yazdani, R., M. Askari, A.M. Ahmadi, G. Azizi, B. Ciric, A. Boehm, G.X. Zhang, and A. Rostami.
1092 2024. Mouse monocytes express CD127 by immune cells, not LPS. *Front Immunol* 15:1356004.

1093 Zhang, B., Y. Zhang, L. Xiong, Y. Li, Y. Zhang, J. Zhao, H. Jiang, C. Li, Y. Liu, X. Liu, H. Liu, Y.F.
1094 Ping, Q.C. Zhang, Z. Zhang, X.W. Bian, Y. Zhao, and X. Hu. 2022. CD127 imprints functional
1095 heterogeneity to diversify monocyte responses in inflammatory diseases. *J Exp Med* 219:

1096

Acknowledgments: The helpful discussions with Tim Lämmermann, Tatjana Ruhl, Gabriel Sollberger, and all members of the Institute of Molecular and Clinical Immunology are gratefully acknowledged. We thank Tamas Dolowschiak for invaluable advice for setting up the scRNAseq library construction. We also thank Roland Hartig from the MPBIC platform and the team of the ZTL of the Medical Faculty OvGU for excellent technical support, and Ehsan Vafadarnejad for the support with initial scRNAseq data analysis.

Funding: This work was supported by funding from the European Research Council (ERC) under the European Union's Horizon 2020 research and innovation program (StG ImmProDynamics, grant agreement 714233 to A.J.M and grant 677200 to N.J.), the German Research Foundation (DFG) (SFB854-B31, MU3744/6-1, and SPP2225 EXIT (MU3744/5-1)).

Author contributions: YF, TS, AES and AJM conceived of and designed the study. YF, IS, ER, LP, PG, LK, BK, LAD, VD, JA, NJN, MB, IB, JM, JP, CS, BP, and AJM conducted experiments, YF, ER, CT, LP, JM, SK, LK, BK, SF, AB, RG and AJM analyzed the data. NG, TT, BS, HVH, MG, BB, NJ, and TS provided critical technology. YF, TS, AES and AJM wrote the manuscript. All authors revised, commented and approved the manuscript.

Competing interests: The authors declare no competing interests.

Data and materials availability: RNAseq data supporting the findings of this study have been deposited at Gene Expression Omnibus under accession no. GSE228455. R scripts used for the analysis of the scRNAseq data are available on GitHub: https://github.com/saliba-lab/Monocytes_leishmania

1122 **Figure legends**

1123

1124 **Figure 1.**

1125 **PDPN^{+}IL-7R^{+} phagocytes infected with low proliferating *L. major* exhibit a hypo-inflammatory**

1126 **phenotype.**

1127 **A.** Experimental setup for *in vivo L. major* proliferation measurement using *Lm*^{SWITCH}. **B.** Experimental

1128 setup for index single-cell sorting of CD11c^{int-hi} and Ly6c^{+} monocytes from 10 individual mouse ears

1129 infected with proliferation reporter parasites at 3 weeks post-infection (p.i.). **C.** Index mKikume red and

1130 green reporter fluorescence values. **D.** *L. major* reads detected in the sorted monocytes infected with

1131 high (green) or low (red) proliferating pathogen, or uninfected (black). **E.** UMAP representation and

1132 mapping of cells sorted as high-proliferator infected (green), uninfected (black) and low-proliferator

1133 infected (red). **F.** Leiden clustering of the scRNAseq data on the UMAP representation. **G.** Fraction of

1134 monocytes sorted as infected with *Lm*^{hi} (green), uninfected (black) or infected with *Lm*^{lo} (red) among

1135 the three clusters identified by the Leiden algorithm. The five highlighted most prominent populations

1136 (*Lm*^{hi}Mo1, UMo1, Cluster 1; *Lm*^{hi}Mo2, Umo2, Cluster 2; *Lm*^{lo}Mo3, Cluster 3) were selected for

1137 differentially expressed gene (DEG) analysis. **H.** Normalized expression (color-code) and cell fraction

1138 per population with detected expression (circle size) for selected DEG differentially expressed in

1139 *Lm*^{lo}Mo3 versus all other populations. **I.** Quantitative PCR (qPCR) analysis of selected genes identified

1140 by scRNAseq. Expression levels were determined for replicates of 50-100 cells sorted according to the

1141 gating strategy outlined in fig. S1K. Expression levels relative to *Gapdh* and normalized to *Lm*^{lo}Mo3 are

1142 shown. Each symbol represents 50-100 cell replicates; data was generated from two independent

1143 experiments. Horizontal lines denote the median. ****, $p<0.0001$;***, $p<0.001$;**, $p<0.01$;*, $p<0.05$

1144 compared to the *Lm*^{lo}Mo3 population according to one-way ANOVA with Dunnett's post-test. **J.** Mean

1145 fluorescence intensity (MFI) of pro-IL-1β, CXCL9, IL-6, and IL-12 p35 among the *Lm*^{hi}Mo1, Umo1,

1146 *Lm*^{hi}Mo2, Umo2, and *Lm*^{lo}Mo3 (according to the gating strategy shown in fig. S1K) from *L. major*

1147 infected C56BL/6J mouse ear skin at 3 weeks p.i. Each dot represents one infected ear analyzed, data

1148 pooled from two independent experiments. Horizontal lines denote mean. ****, $p<0.0001$; **, $p<0.01$;

1149 *, $p<0.05$ according to one-way ANOVA multiple comparison with Dunnett's post-test.

1150

1151

1152 **Figure 2. IL-7R^{+}PDPN^{+} *Lm*^{lo}Mo3 develop from bone-marrow derived CCR2^{+} monocytes and**

1153 **acquire their phenotype in the infected tissue.**

1154 **A.** Gating to determine tissue-resident and monocyte-derived dendritic cells (TR/MoDC), tissue-

1155 resident macrophages (TRM) and different monocyte-derived populations (left) and proportion of these

1156 populations among CD11b^{+}Ly6G^{-}SiglecF^{-} phagocytes (right). **B.** Proportion of the cell populations

1157 shown in (A) among *Lm*^{hi}Mo1, Umo1, *Lm*^{hi}Mo2, Umo2, and *Lm*^{lo}Mo3 (H) and among infected

1158 CD11b^{+}Ly6G^{-}SiglecF^{-} cells with differential PDPN and IL-7R expression and different intracellular

1159 pathogen proliferation rates. Horizontal lines denote the median. Each dot represents one infected ear

1160 analyzed, data pooled from two independent experiments. **C.** Experimental approach to identify newly

1161 recruited monocytes by photoconversion of mKikume transgenic mice (left). **D.** Upper left: Infected

1162 CD11b^{+}Ly6G^{-}SiglecF^{-} cells from *Lm*^{Turquoise}-infected ear tissue at 3 weeks p.i. from mKikume transgenic

1163 mice before (green curve) and 0 h after photoconversion (red curve). Lower left: Identification of short

1164 resident mKikume green (recruited <5 days after photoconversion) and long resident mKikume red

1165 (recruited >5 days after photoconversion) cells among infected CD11b^{+}Ly6G^{-}SiglecF^{-} cells. Right:

1166 Examples of the proportion long resident cells (mKikume red^{+}) among infected CD11b^{+}Ly6G^{-}SiglecF^{-}

1167 cells with differential PDPN and IL-7R expression. **E.** Quantification of short and long resident cells

1168 among infected CD11b^{+}Ly6G^{-}SiglecF^{-} cells with differential PDPN and IL-7R expression. Horizontal

1169 lines denote the median. Each dot represents one infected analyzed ear, data pooled from two

1170 independent experiments. **F.** Experimental approach to demonstrate the origin of *Lm*^{lo}Mo3 from bone

1171 marrow-derived, CCR2^{+} monocytes recruited during the innate and adaptive phase of the anti-

1172 *Leishmania* response. **G.** CCR2-cre^{ER}-dependent TdTomato expression in different blood leukocytes

1173 cells before, and at day 2, 6 and 23 after the beginning of five daily Tamoxifen injections. Horizontal

1174 lines denote the median. Each dot represents one animal, data pooled from two independent experiments.

1175 **H.** Fraction of CCR2-cre^{ER}-dependent tdTomato expressing cells among PDPN and IL-7R expressing

1176 monocyte-derived cells. The cre recombinase activity was induced in CCR2^{+} monocytes for the innate

1177 phase of the immune response by injecting Tamoxifen before infection (left), or for the adaptive phase

1178 by injection at 11-15 days p.i. (right). Horizontal lines denote the median. Each symbol represents one
1179 infection site per condition obtained from two independent experiments.
1180
1181 **Figure 3. PDPN$^+$IL-7R$^+$ *Lm*^{lo}Mo3 dampen T cell responses against *L. major* infection *in vivo*.**
1182 **A**. Proportion of PDPN$^-$IL-7R$^+$ (left), PDPN$^+$ IL-7R$^-$ (middle) and PDPN$^+$IL-7R$^+$ (right) fractions among
1183 different leukocytes at the infection site at week 3 p.i. Bars denote the median. Each symbol represents
1184 one infection site per condition obtained from two independent experiments. **B.** Experimental setup for
1185 cell-specific *Il7r*-deficiency in PDPN$^+$ leukocytes. **C.** Validation of cell-specific IL-7R deficiency.
1186 Upper panels: Example and MFI analysis for IL-7R surface expression on *Lm*^{lo}Mo3 (gated according to
1187 figure S1K) in the infected ear tissue at 3 weeks p.i. Lower panels: Example and MFI analysis of IL-7R
1188 expression on CD4$^+$ T cells in the draining lymph node (dLN) at week 3 p.i. Values are normalized to
1189 control animals. Each dot represents one infected ear or dLN analyzed. Isotype control-stained samples
1190 are shown as a grey histogram and dashed line in the data plot, respectively. Horizontal lines denote
1191 mean, data pooled from 2 independent experiments. **, $p<0.01$; ns, not significant according to unpaired
1192 t-test. **D.** *L. major*-infected cell fraction among recruited monocytes in the ear tissue (left) and limiting
1193 dilution assay (LDA) of *L. major* tissue burden normalized to control animals (right) at week 3 p.i. of
1194 lethally irratiated mice either reconstituted with littermate control (black symbols) or *Pdpn-cre* × *Il7r*$^{fl/fl}$
1195 BM (blue symbols). **E.** IFNγ$^+$ fraction and IFNγ MFI among effector CD4$^+$ T cells within *L. major*-
1196 infected ear at week 3 p.i.for mice reconstituted with either littermate control (black symbols) or *Pdpn-*
1197 *cre* × *Il7r*$^{fl/fl}$ BM (blue symbols). Each symbol in (D-E) represents one individual mouse ear. Horizontal
1198 lines denote the mean. ***, $p<0.001$; **, $p<0.01$; *, $p<0.05$ according to unpaired t-test. Data
1199 representative of two independent experiments. **F.** Experimental setup for mixed BM chimera
1200 reconstituted with 50% CD45.1 WT and 50% *Il7r*$^{-/-}$ (CD45.2) BM. Mice reconstituted with mixtures of
1201 WT CD45.1 and WT CD45.2 BM served as controls. **G.** *L. major* infected cell fraction among recruited
1202 monocytes in the ear tissue at week 3 p.i., either WT BM chimera compartment (black symbols), or *Il7r*$^-$
1203 $^{/-}$ BM chimera compartment (blue symbols). **H.** Fraction of *Lm*^{hi}Mo1, *Lm*^{hi}Mo2, and *Lm*^{lo}Mo3 (gated
1204 according to figure S1K) among monocyte-derived cells of each BM chimera compartment, either WT
1205 BM chimera compartment (closed symbols), or *Il7r*$^{-/-}$ BM chimera compartment (open symbols) within

1206 *L. major* infected ear tissue at 3 week p.i. Each symbol represents one individual mouse ear, data pooled
1207 from two independent experiments. Horizontal lines denote the median. No significance detected
1208 according to one-way ANOVA multiple comparison with Dunn's post-test. **I**. Intracellular pathogen
1209 proliferation rates among *Lm*^{hi}Mo1, *Lm*^{hi}Mo2, and *Lm*^{lo}Mo3 (gated according to figure S1K), either WT
1210 BM chimera compartment (closed symbols), or *Il7r*$^{-/-}$ BM chimera compartment (open symbols). Each
1211 symbol represents one individual mouse ear, data pooled from two independent experiments. Horizontal
1212 lines denote the median. ****, $p<0.0001$ according to one-way ANOVA multiple comparison with
1213 Dunnett post-test. **J.** Experimental setup for depletion of *Pdpn*-expressing leukocytes of lethally
1214 irradiated mice reconstituted with either *Pdpn-cre* × iDTR BM cells, or 50% of *Pdpn-cre* × iDTR and
1215 50% of CD45.1 WT BM cells. **K.** Validation of depletion of PDPN^{+} cells among infected leukocytes.
1216 Upper panel: Example of PDPN staining of infected cells from ear tissue at 3 weeks p.i. in depleted
1217 (blue curve) or non-depleted control animals (black curve). Lower panel: Percentage of PDPN^{+} cells
1218 among infected leukocytes from ear tissue at 3 weeks p.i. in depleted (blue symbols) or non-depleted
1219 control animals (black symbols). Horizontal lines denote the mean. Each dot represents one infected ear
1220 analyzed. *, $p<0.05$; ns, not significant according to unpaired t-test. **L.** *L. major* infected phagocyte
1221 fraction (left) and *L. major* burden (right, normalized to non-depleted control) in the ear at week 3 p.i.
1222 in non-depleted (black symbols) or partially depleted (grey symbols) controls versus 100% *Pdpn*-
1223 dependent depleted BM chimeras (blue symbols). **M.** Fraction (left) and MFI (right) of IFNγ^{+} expressing
1224 CD4^{+}CD44^{+} effector T cells from ear tissue (left) in the ear at week 3 p.i. in non-depleted (black
1225 symbols) or partially depleted (grey symbols) controls versus 100% *Pdpn*-dependent depleted BM
1226 chimeras (blue symbols). Each symbol in (L) and (M) represents one individual mouse ear, data
1227 representative of two independent experiments. Horizontal lines denote the median. **, $p<0.01$
1228 according to Mann-Whitney test.
1229
1230 **Figure 4. Fibroblast-produced IL-7 contributes to pathogen persistence and suppression of IFNγ**
1231 **production in effector T cells.**
1232 **A.** Upper panels: H2KB^{+} or PD-L1^{+} fraction and H2KB or PD-L1 MFI of among fibroblasts from mice
1233 reconstituted with *Pdpn-cre* × *Il7r*$^{WT/WT}$ littermate control BM (black symbols) or *Pdpn-cre* × *Il7r*$^{fl/fl}$ BM

1234 (blue symbols). Data normalized to mice reconstituted with littermate control BM. Lower panels:
1235 H2KB$^+$ or PD-L1$^+$ fraction and H2KB or PD-L1 MFI of among fibroblasts from non-depleted control
1236 (black symbols) or *Pdpn*-dependent 100% depleted (blue symbols) ear infections. Each symbol
1237 represents one individual mouse ear. Data normalized to non-depleted control animals. Horizontal lines
1238 denote the mean. ***, p<0.001; **, p<0.01; *, p<0.05 according to unpaired t-test. Data shown
1239 correspond to the experiments shown in fig. 3C-E, , and K, respectively. **B.** Expression of *Il7* within *L.*
1240 *major*-infected (week 3 p.i.) and non-infected ear tissue. Expression as determined by ΔΔCT between
1241 *Il7* and *Hprt* qPCR. CT values are corrected according to the mean difference in RNA extracted (see fig.
1242 S5C). Each symbol represents one individual mouse ear. Horizontal lines denote the mean. *, p<0.05
1243 according to unpaired t-test. **C.** Expression level of *Prrx* among fibroblasts, LEC, BEC and PDPN$^-$CD31$^-$
1244 non-immune cells within *L. major*-infected ear tissue at week 3 p.i.. Expression as determined by ΔΔCT
1245 between *Prrx* and *Hprt* qPCR followed by normalization to PDPN$^-$CD31$^-$ cells. Each symbol represents
1246 one individual mouse ear. Horizontal lines denote the mean. ****, p<0.0001 according to one-way
1247 ANOVA multiple comparison with Dunnett's post-test. Data in (A-C) pooled from two independent
1248 experiments. **D.** Proportion of fibroblasts, LEC, and BEC among CD45$^-$TER119$^-$7AAD$^-$ cells within the
1249 *L. major* infected ear at week 3 p.i.. Each symbol represents one individual mouse ear. Horizontal lines
1250 denote the mean. ****, p<0.0001 according to one-way ANOVA multiple comparison with Dunnett's
1251 post-test. **E.** Experimental setup to test for *Prrx*-expressing fibroblasts as a necessary source of IL-7 to
1252 promote *Lm*^{lo}Mo3 mediated suppression of CD4$^+$ T cell responses in the *L. major* infected ear tissue. **F.**
1253 Expression level of *Il7* among fibroblasts, LEC, and BEC within *L. major*-infected ear tissue from
1254 littermate control (*Prrx-Cre* × *Il7*$^{wt/wt}$) (black symbols) and *Prrx-cre* × *Il7*$^{fl/fl}$ (blue symbols). Expression
1255 as determined by ΔCT between *Il7* and *Hprt* qPCR. **G.** Left: the fraction of *L. major* infected cells
1256 among recruited monocytes in the ear tissue at week 3 p.i., littermate control (*Prrx-Cre* × *Il7*$^{wt/wt}$) (filled
1257 symbols) and *Prrx-cre* × *Il7*$^{fl/fl}$ (open symbols). Differently shaded symbols represent two independent
1258 experiments. Each symbol represents one individual mouse ear. Horizontal lines denote the median.
1259 ***, p<0.001 according to two-way ANOVA comparing genotypes. Right: Limiting dilution assay
1260 (LDA) of *L. major* tissue burden in the ear. Data normalized to littermate control animals. **H.** IFNγ$^+$
1261 fraction and MFI of IFNγ signal among effector CD4$^+$ T cells within *L. major*-infected ear at week 3 p.i.

1262 of either littermate control (black symbols) or *Prrx-cre* × *Il7*$^{fl/fl}$ animals (blue symbols). Data normalized
1263 to littermate control animals. Each symbol in (G-I) represents one individual mouse ear, data are from
1264 two independent experiments. Horizontal lines denote the mean. *, $p<0.05$ according to unpaired t-test.
1265

1266 **Figure 5. IFNγ activates fibroblasts to produce IL-7 depending of the infection amplitude.**
1267 **A**. Proportion of IFNγ^{+} produced by T, NK, and dendritic cells at week 3 p.i. Each symbol represents
1268 one individual mouse ear. Horizontal lines denote the mean. ****, $p<0.0001$ according to unpaired t-
1269 test. **B.** Expression of the *Il7* cytokine gene in ex vivo cultivated fibroblasts without (black symbols) and
1270 with (red symbols) addition of IFNγ^{+} for 24h. Horizontal lines denote the median. **, $p<0.01$ according
1271 to Mann-Whitney test. **C.** Experimental setup to test the impact of anti-IFNγ treatment in fibroblasts
1272 within an ongoing *L. major* infection. **D.** Correlation (r^2, with p value indicated) and linear regression
1273 (red line) between *L. major* infection rate (determined by flow cytometry) and *Il7* expression level
1274 (qPCR) in fibroblasts within the infected ear (week 3 p.i.), in either isotype control (black symbols,
1275 upper graph) or anti-IFNγ treated (orange symbols, lower graph) animals. Each symbol represents one
1276 replicate of flow cytometry analysis from six individual infected ears per condition with qPCR of up to
1277 3 pools of 200 fibroblasts sorted from the same infected ear. The vertical dashed line shows the threshold
1278 defined for analyzing highly infected tissues. **E.** Comparison of *Il7* expression in fibroblasts sorted from
1279 tissues with an infection rate above the threshold (dashed line) shown in (D). **F.** H2KB^{+} or PD-L1^{+}
1280 fraction and H2KB or PD-L1 MFI among fibroblasts isolated from week 3 p.i. infected ears of animals
1281 treated with either isotype control (black symbols) or anti-IFNγ antibody (orange symbols). Each symbol
1282 in (E-G) represents one individual mouse ear, horizontal lines denote the mean. ***, $p<0.001$; **,
1283 $p<0.01$; *, $p<0.05$ according to unpaired t-test. Data were collected in two independent experiments.
1284

1285 **Figure 6. Anti-IL-7/IL-7R treatment results in an enhanced immune response against *L. major*.**
1286 **A.** Hypothesis (box) and experimental setup for testing the effects of anti-IL-7/IL-7R treatment during
1287 *L. major* infection. Treatment was applied twice (day 16, 20, black arrows, data shown in panel B-F) or
1288 once (day 18, grey arrow, data shown in panel C). **B-C.** Limiting dilution assay (LDA) of *L. major* tissue
1289 burden in the ear following anti-IL-7/IL-7R treatment normalized to isotype control treated animals (B)

1290 and *L. major* infected cell fraction among recruited monocytes with two-dosage (left panel) or single-
1291 dosage anti-IL-7/IL-7R treatment (right panel) (C). **D.** IFNγ$^+$ fraction (left) and IFNγ MFI (normalized
1292 to isotype control treatment, right) among effector CD4$^+$ T cells isolated from the ears at week 3 p.i. of
1293 either isotype antibody (black symbols) or anti-IL-7R/IL-7 treated animals (blue symbols). **E.** H2KB$^+$
1294 and PD-L1$^+$ fraction among fibroblasts, and the MFI of H2KB or PD-L1 among fibroblasts (normalized
1295 to isotype control animals), either isotype control (black symbols) or anti-IL-7R/IL-7 treated (blue
1296 symbols). **F.** iNOS$^+$ fraction and iNOS MFI (normalized to isotype control animals) among total
1297 recruited monocyte-derived cells (left panel) and infected monocyte-derived cells (right panel), either
1298 isotype control (black symbols) or anti-IL-7R/IL-7 treated samples (blue symbols). Each symbol in (B-
1299 F) represents one individual mouse ear, data pooled from two independent experiments. Horizontal lines
1300 denote the mean. . **, $p<0.01$; *, $p<0.05$ according to unpaired t-test. **G**. Experimental setup to determine
1301 the long-term effects of anti-IL-7/IL-7R treatment. **H.** Infection-associated immune cell recruitment
1302 determined by ear diameter of isotype control-treated (grey) and anti-IL-7/IL-7R treated (blue) animals.
1303 Data were normalized to the mean of the corresponding values of the same ear measured before the
1304 treatment. Bars denote the mean+SD. Each symbol represents one individual ear repeatedly measured
1305 throughout the infection time course. Data obtained from two independent experiments. ****, $p<0.0001$
1306 *, $p<0.05$ according to 2-way ANOVA (treatment, experiment) with Bonferroni post-test. **I.** Limiting
1307 dilution assay (LDA) of *L. major* tissue burden in the ear at week 7 p.i. of animals previously treated
1308 (week 3 p.i.) with isotype control-treated (black symbols) or anti-IL-7/IL-7R treated (blue symbols). **J.**
1309 IFNγ$^+$ fraction among CD4$^+$ T cells isolated from the draining lymph node at week 7 p.i. of animals
1310 previously treated (week 3 p.i.) with either isotype control (black symbols) or anti-IL-7R/IL-7 antibody
1311 (blue symbols). Each symbol in (I-J) represents one individual ear. Data pooled from two independent
1312 experiments and normalized to control animals of each experiment for limiting dilution. Horizontal lines
1313 denote the median. *, $p<0.05$ according unpaired Mann-Whitney test. Each symbol represents one
1314 individual mouse ear. Horizontal lines denote the mean. ***, $p<0.001$; according to unpaired Mann-
1315 Whitney test.
1316
1317

Figure 1

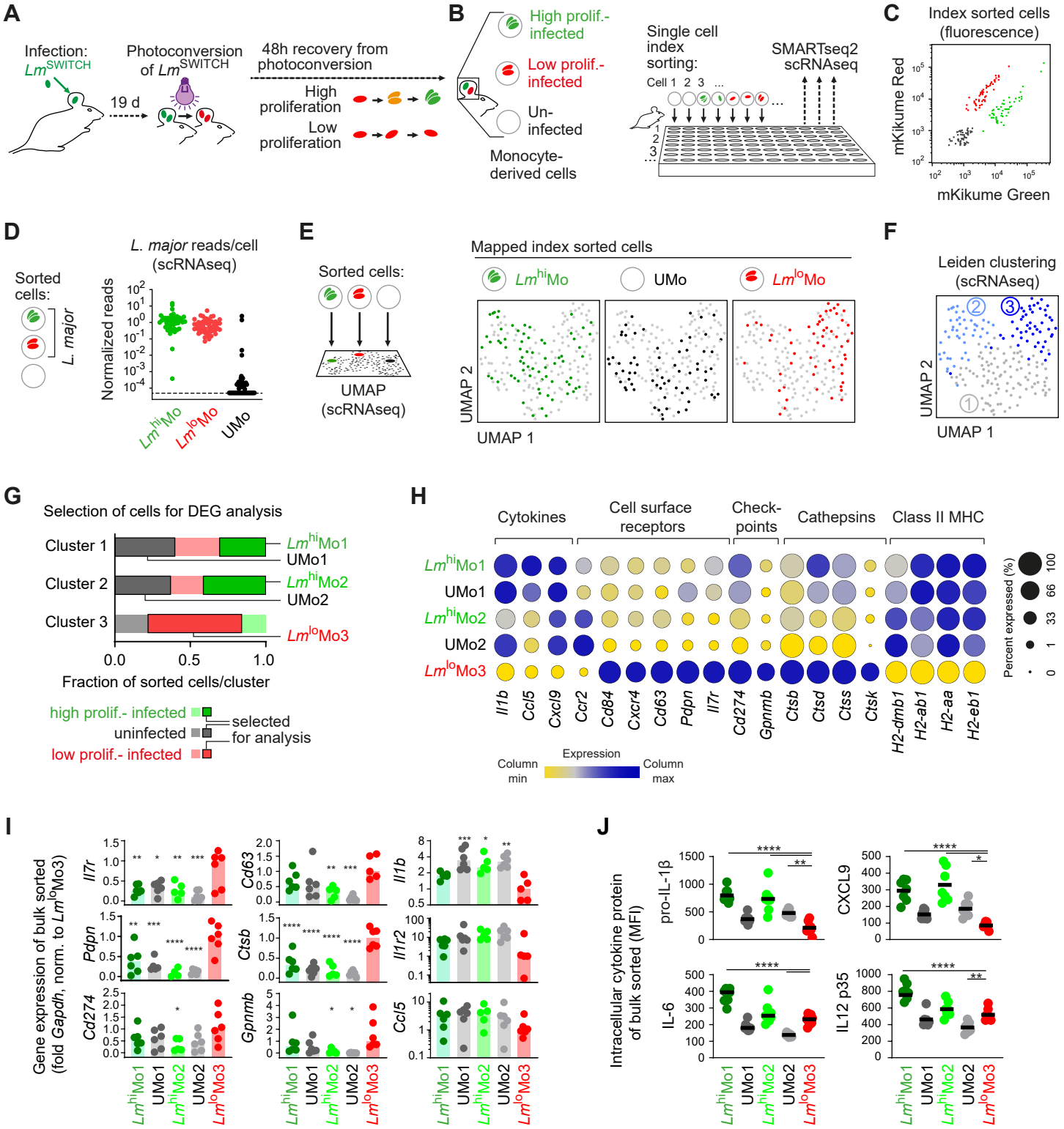
A
Infection:
Lm SWITCH
19 d
Photoconversion of Lm SWITCH
48h recovery from photoconversion
High proliferation
Low proliferation
B
High prolif.- infected
Low prolif.- infected
Un- infected
Monocyte- derived cells
Single cell index sorting:
Cell 1 2 3 ...
SMARTseq2 scRNAseq
C
Index sorted cells (fluorescence)
mKikume Red
mKikume Green
D
Sorted cells:
L. major
L. major reads/cell (scRNAseq)
Normalized reads
Lm hiMo
Lm loMo
UMo
E
Sorted cells:
UMAP (scRNAseq)
Mapped index sorted cells
Lm hiMo
UMo
Lm loMo
UMAP 2
UMAP 1
F
Leiden clustering (scRNAseq)
UMAP 2
UMAP 1
G
Selection of cells for DEG analysis
Cluster 1
Cluster 2
Cluster 3
Lm hiMo1
UMo1
Lm hiMo2
UMo2
Lm loMo3
Fraction of sorted cells/cluster
high prolif.- infected
uninfected
low prolif.- infected
selected for analysis
H
Cytokines
Cell surface receptors
Check- points
Cathepsins
Class II MHC
Lm hiMo1
UMo1
Lm hiMo2
UMo2
Lm loMo3
Il1b
Ccl5
Cxcl9
Ccr2
Cd84
Cxcr4
Cd63
Pdpn
Il7r
Cd274
Gpnmb
Ctsb
Ctsd
Ctss
Ctsk
H2-dmb1
H2-ab1
H2-aa
H2-eb1
Percent expressed (%)
Expression
Column min
Column max
I
Gene expression of bulk sorted (fold Gapdh, norm. to Lm loMo3)
Il7r
Cd63
Il1b
Pdpn
Ctsb
Il1r2
Cd274
Gpnmb
Ccl5
Lm hiMo1
UMo1
Lm hiMo2
UMo2
Lm loMo3
J
Intracellular cytokine protein of bulk sorted (MFI)
pro-IL-1β
CXCL9
IL-6
IL12 p35

Figure 2

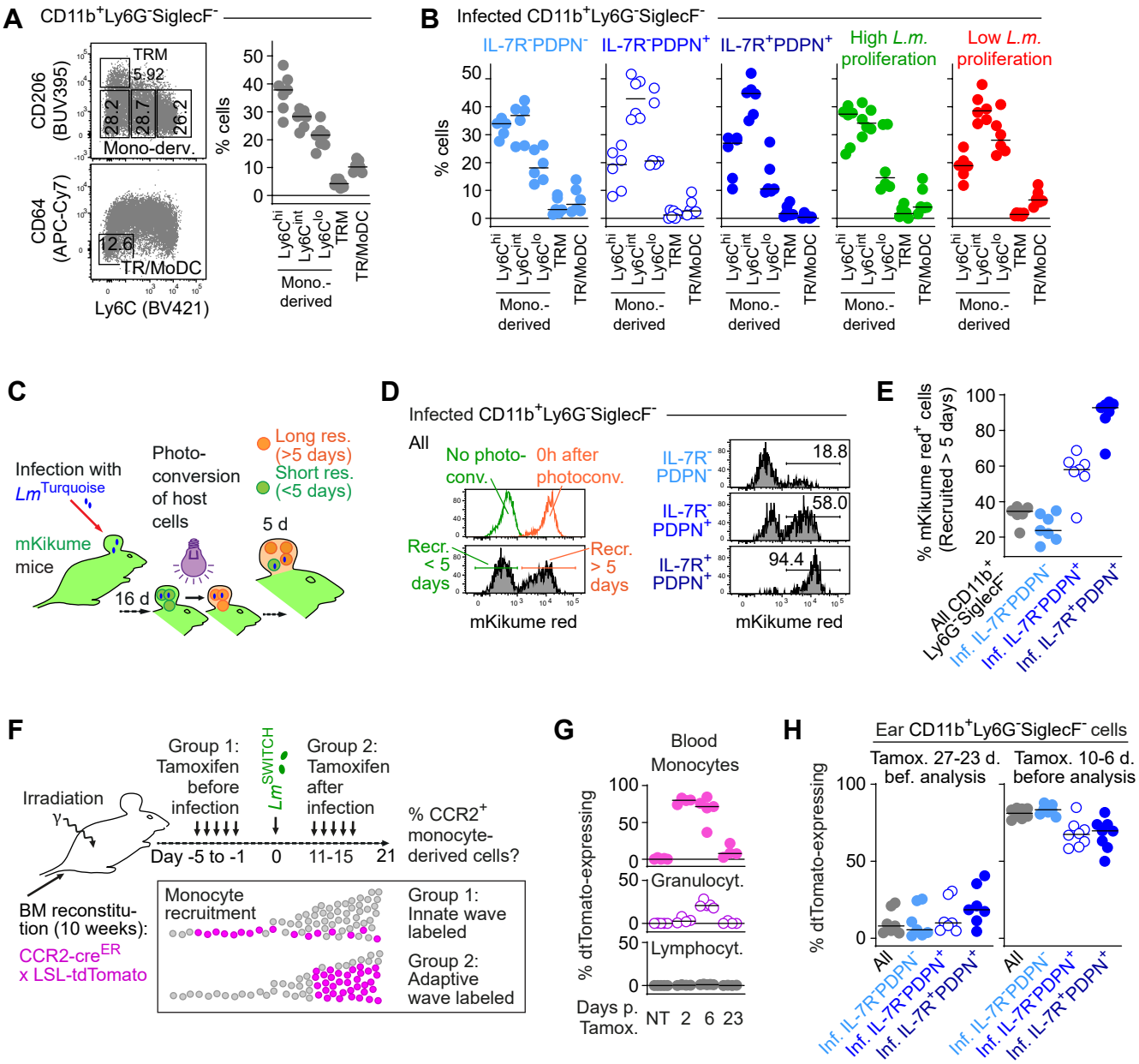
A
CD11b+Ly6G-SiglecF-
CD206 (BUV395)
TRM
5.92
28.2
28.7
26.2
Mono-derv.
CD64 (APC-Cy7)
12.6
TR/MoDC
Ly6C (BV421)
% cells
Ly6Chi
Ly6Cint
Ly6Clo
TRM
TR/MoDC
Mono.-derived
B
Infected CD11b+Ly6G-SiglecF-
IL-7R-PDPN-
IL-7R-PDPN+
IL-7R+PDPN+
High L.m. proliferation
Low L.m. proliferation
C
Infection with
LmTurquoise
mKikume mice
Photo-conversion of host cells
Long res. (>5 days)
Short res. (<5 days)
5 d
16 d
D
Infected CD11b+Ly6G-SiglecF-
All
No photo-conv.
0h after photoconv.
Recr. < 5 days
Recr. > 5 days
IL-7R- PDPN-
IL-7R- PDPN+
IL-7R+ PDPN+
18.8
58.0
94.4
mKikume red
E
% mKikume red+ cells (Recruited > 5 days)
All CD11b+ Ly6G-SiglecF-
Inf. IL-7R-PDPN-
Inf. IL-7R-PDPN+
Inf. IL-7R+PDPN+
F
Irradiation
γ
BM reconstitution (10 weeks):
CCR2-creER x LSL-tdTomato
Group 1: Tamoxifen before infection
LmSWITCH
Group 2: Tamoxifen after infection
Day -5 to -1
0
11-15
21
% CCR2+ monocyte-derived cells?
Monocyte recruitment
Group 1: Innate wave labeled
Group 2: Adaptive wave labeled
G
Blood Monocytes
Granulocyt.
Lymphocyt.
% dtTomato-expressing
Days p. Tamox.
NT
2
6
23
H
Ear CD11b+Ly6G-SiglecF- cells
Tamox. 27-23 d. bef. analysis
Tamox. 10-6 d. before analysis
% dtTomato-expressing
All
Inf. IL-7R-PDPN-
Inf. IL-7R-PDPN+
Inf. IL-7R+PDPN+

Figure 3

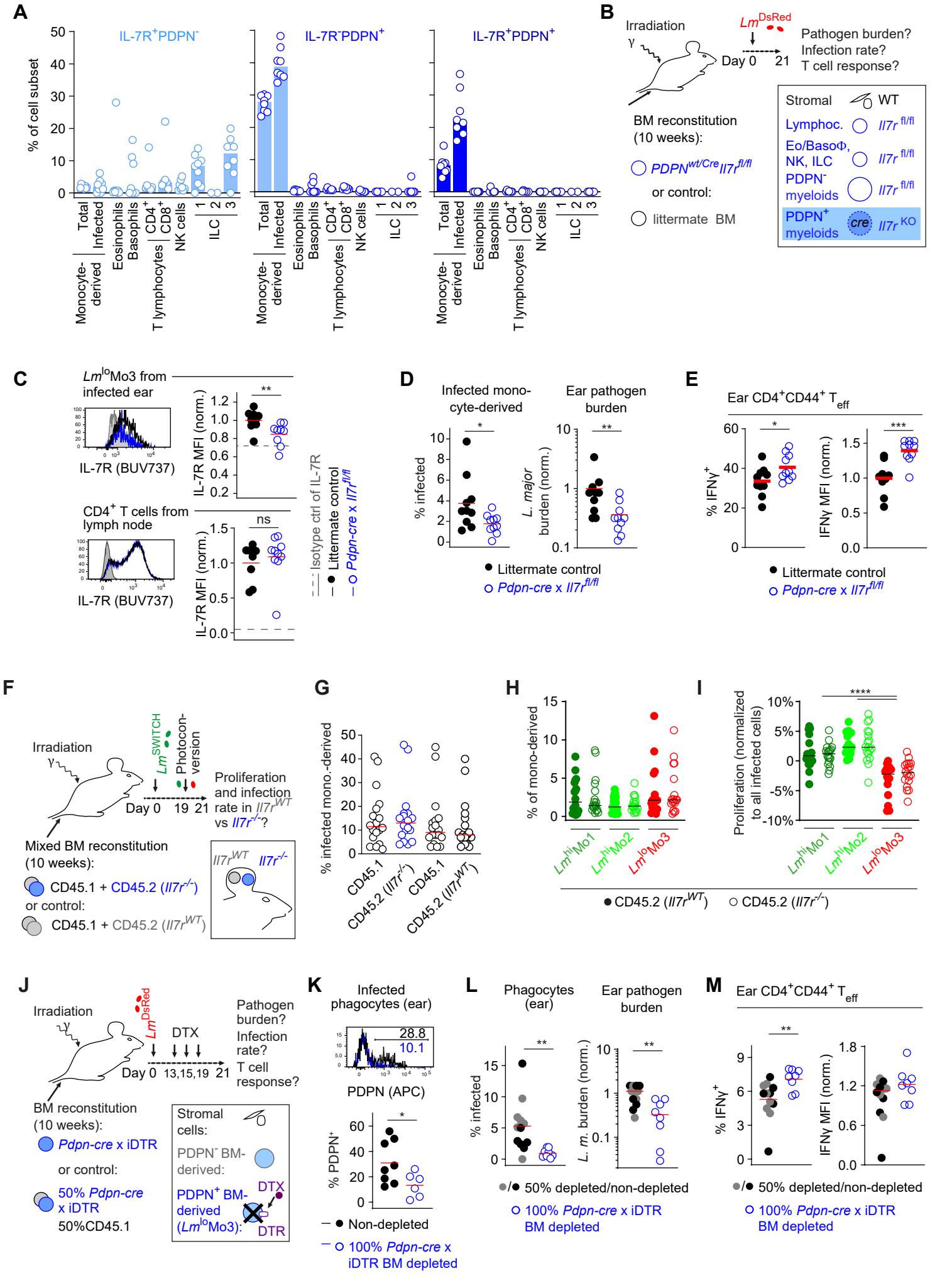
A
IL-7R+PDPN-
IL-7R-PDPN+
IL-7R+PDPN+
% of cell subset
Total
Infected
Monocyte-derived
Eosinophils
Basophils
T lymphocytes
CD4+
CD8+
NK cells
ILC
1
2
3
B
Irradiation
γ
LmDsRed
Day 0
21
Pathogen burden?
Infection rate?
T cell response?
BM reconstitution (10 weeks):
PDPNwt/Cre Il7rfl/fl
or control:
littermate BM
Stromal
WT
Lymphoc.
Il7r fl/fl
Eo/BasoΦ, NK, ILC
PDPN- myeloids
PDPN+ myeloids
cre
Il7r KO
C
LmloMo3 from infected ear
IL-7R (BUV737)
IL-7R MFI (norm.)
**
CD4+ T cells from lymph node
ns
Isotype ctrl of IL-7R
Littermate control
Pdpn-cre x Il7rfl/fl
D
Infected mono-cyte-derived
Ear pathogen burden
% infected
L. major burden (norm.)
*
**
Littermate control
Pdpn-cre x Il7rfl/fl
E
Ear CD4+CD44+ Teff
% IFNγ+
IFNγ MFI (norm.)
*
***
Littermate control
Pdpn-cre x Il7rfl/fl
F
Irradiation
γ
LmSWITCH
Photocon-version
Day 0
19
21
Proliferation and infection rate in Il7rWT vs Il7r-/-?
Mixed BM reconstitution (10 weeks):
CD45.1 + CD45.2 (Il7r-/-)
or control:
CD45.1 + CD45.2 (Il7rWT)
Il7rWT
Il7r-/-
G
% infected mono.-derived
CD45.1
CD45.2 (Il7r-/-)
CD45.1
CD45.2 (Il7rWT)
H
% of mono-derived
LmhiMo1
LmhiMo2
LmloMo3
CD45.2 (Il7rWT)
CD45.2 (Il7r-/-)
I
Proliferation (normalized to all infected cells)
****
LmhiMo1
LmhiMo2
LmloMo3
CD45.2 (Il7rWT)
CD45.2 (Il7r-/-)
J
Irradiation
γ
LmDsRed
DTX
Day 0
13,15,19
21
Pathogen burden?
Infection rate?
T cell response?
BM reconstitution (10 weeks):
Pdpn-cre x iDTR
or control:
50% Pdpn-cre x iDTR
50%CD45.1
Stromal cells:
PDPN- BM-derived:
PDPN+ BM-derived (LmloMo3):
DTX
DTR
K
Infected phagocytes (ear)
28.8
10.1
PDPN (APC)
% PDPN+
*
Non-depleted
100% Pdpn-cre x iDTR BM depleted
L
Phagocytes (ear)
Ear pathogen burden
% infected
L. m. burden (norm.)
**
**
50% depleted/non-depleted
100% Pdpn-cre x iDTR BM depleted
M
Ear CD4+CD44+ Teff
% IFNγ+
IFNγ MFI (norm.)
**
50% depleted/non-depleted
100% Pdpn-cre x iDTR BM depleted

Figure 4

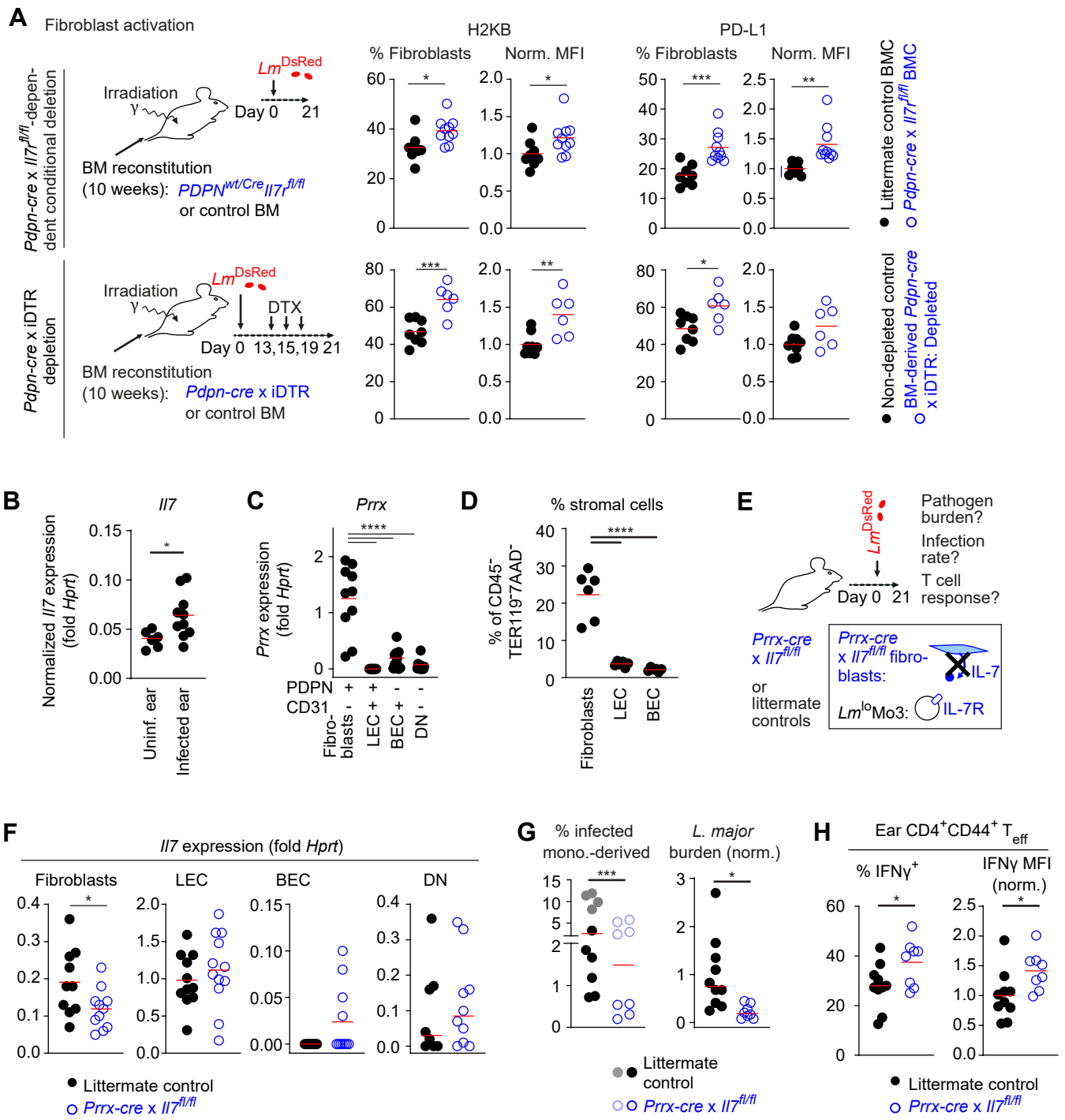
A
Fibroblast activation
H2KB
PD-L1
% Fibroblasts
Norm. MFI
Pdpn-cre x Il7r fl/fl-dependent conditional deletion
Irradiation
γ
Lm DsRed
Day 0
21
BM reconstitution
(10 weeks): PDPN wt/Cre Il7r fl/fl
or control BM
Littermate control BMC
Pdpn-cre x Il7r fl/fl BMC
Pdpn-cre x iDTR depletion
DTX
Day 0 13,15,19 21
Pdpn-cre x iDTR
Non-depleted control
BM-derived Pdpn-cre x iDTR: Depleted
B
Il7
Normalized Il7 expression (fold Hprt)
Uninf. ear
Infected ear
C
Prrx
Prrx expression (fold Hprt)
PDPN
CD31
Fibro-blasts
LEC
BEC
DN
D
% stromal cells
% of CD45- TER119-7AAD-
Fibroblasts
LEC
BEC
E
Pathogen burden?
Infection rate?
T cell response?
Prrx-cre x Il7 fl/fl
or littermate controls
Prrx-cre x Il7 fl/fl fibro-blasts:
IL-7
Lm loMo3:
IL-7R
F
Il7 expression (fold Hprt)
Fibroblasts
LEC
BEC
DN
Littermate control
Prrx-cre x Il7 fl/fl
G
% infected mono.-derived
L. major burden (norm.)
Littermate control
Prrx-cre x Il7 fl/fl
H
Ear CD4+CD44+ Teff
% IFNγ+
IFNγ MFI (norm.)
Littermate control
Prrx-cre x Il7 fl/fl

Figure 5

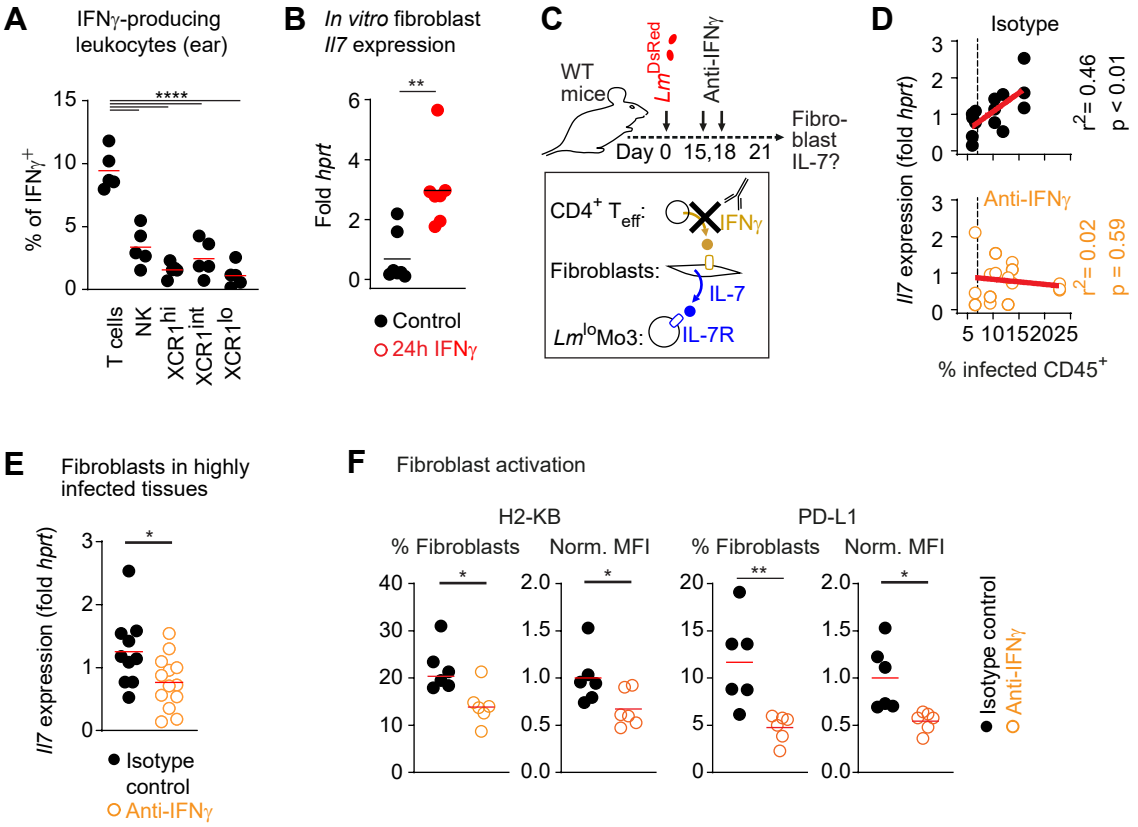
A
IFNγ-producing leukocytes (ear)
% of IFNγ+
****
T cells
NK
XCR1hi
XCR1int
XCR1lo
B
In vitro fibroblast Il7 expression
Fold hprt
**
Control
24h IFNγ
C
WT mice
LmDsRed
Anti-IFNγ
Day 0 15,18 21
Fibro-blast IL-7?
CD4+ Teff:
IFNγ
Fibroblasts:
IL-7
LmloMo3:
IL-7R
D
Isotype
Anti-IFNγ
Il7 expression (fold hprt)
r2= 0.46
p < 0.01
r2= 0.02
p = 0.59
% infected CD45+
E
Fibroblasts in highly infected tissues
Il7 expression (fold hprt)
*
Isotype control
Anti-IFNγ
F
Fibroblast activation
H2-KB
PD-L1
% Fibroblasts
Norm. MFI
Isotype control
Anti-IFNγ

Figure 6

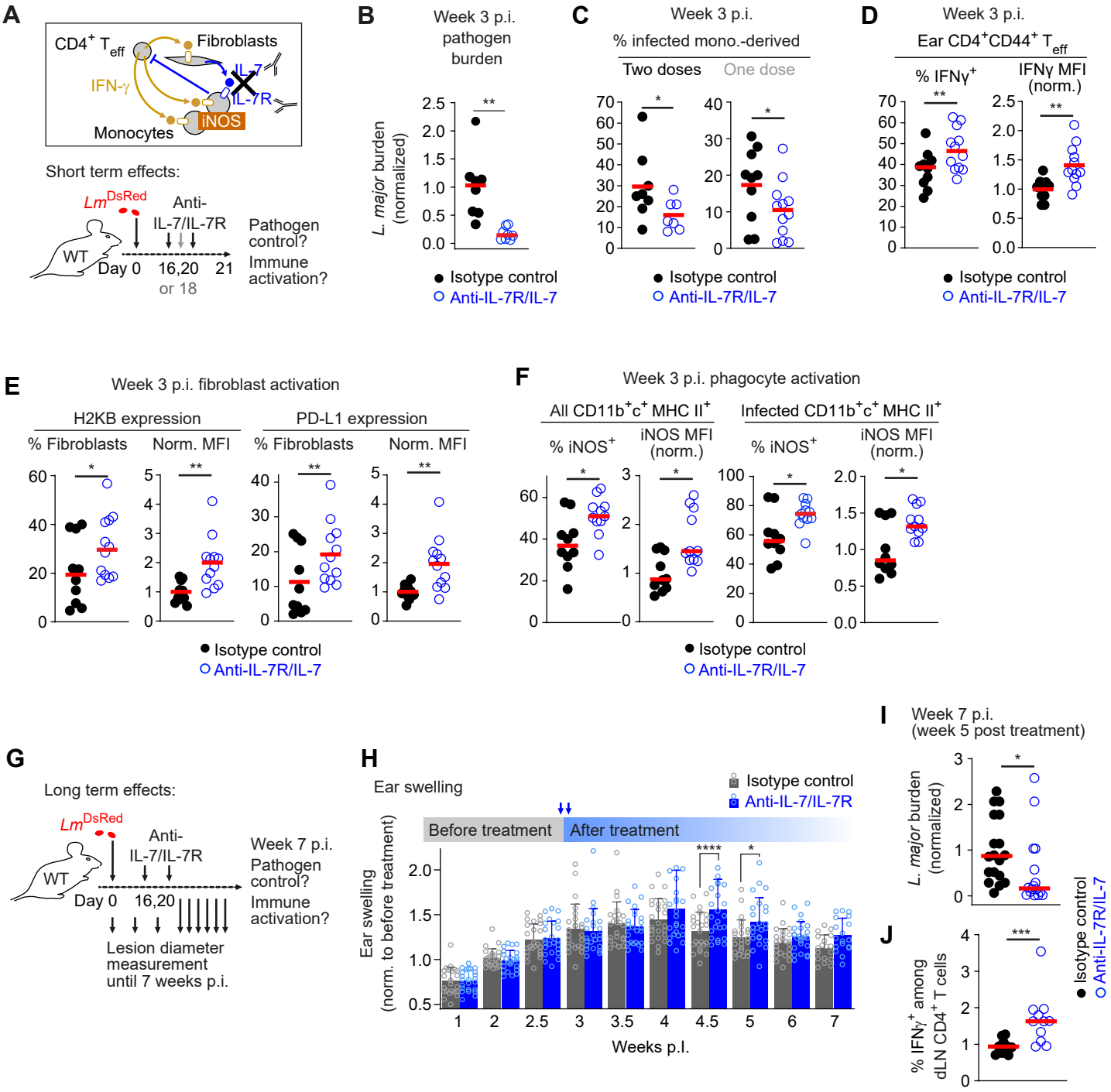
A
CD4+ Teff
Fibroblasts
IL-7
IFN-γ
IL-7R
iNOS
Monocytes
Short term effects:
LmDsRed
Anti-
IL-7/IL-7R
WT
Day 0
16,20
or 18
21
Pathogen control?
Immune activation?
B
Week 3 p.i.
pathogen burden
L. major burden (normalized)
Isotype control
Anti-IL-7R/IL-7
C
Week 3 p.i.
% infected mono.-derived
Two doses
One dose
Isotype control
Anti-IL-7R/IL-7
D
Week 3 p.i.
Ear CD4+CD44+ Teff
% IFNγ+
IFNγ MFI (norm.)
Isotype control
Anti-IL-7R/IL-7
E
Week 3 p.i. fibroblast activation
H2KB expression
PD-L1 expression
% Fibroblasts
Norm. MFI
% Fibroblasts
Norm. MFI
Isotype control
Anti-IL-7R/IL-7
F
Week 3 p.i. phagocyte activation
All CD11b+c+ MHC II+
Infected CD11b+c+ MHC II+
% iNOS+
iNOS MFI (norm.)
% iNOS+
iNOS MFI (norm.)
Isotype control
Anti-IL-7R/IL-7
G
Long term effects:
LmDsRed
Anti-
IL-7/IL-7R
WT
Day 0
16,20
Week 7 p.i.
Pathogen control?
Immune activation?
Lesion diameter measurement until 7 weeks p.i.
H
Ear swelling
Isotype control
Anti-IL-7/IL-7R
Before treatment
After treatment
Ear swelling (norm. to before treatment)
Weeks p.i.
I
Week 7 p.i.
(week 5 post treatment)
L. major burden (normalized)
J
% IFNγ+ among dLN CD4+ T cells
Isotype control
Anti-IL-7R/IL-7